Title
Dynamic Behavior of a Premixed Turbulent Open V-Flame

Authors
Rhee, C.W.
Talbot, L.
Sethian, J.A.

Publication Date
1994

LBL-35188
UC-400
Preprint

Lawrence Berkeley Laboratory

UNIVERSITY OF CALIFORNIA

ENERGY & ENVIRONMENT DIVISION

Submitted to Journal of Fluid Mechanics

Dynamical Behavior of a Premixed Turbulent Open V-Flame

C.W. Rhee, L. Talbot, and J.A. Sethian

January 1994

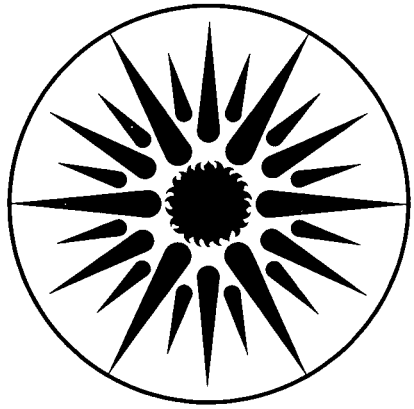

ENERGY & ENVIRONMENT DIVISION

Prepared for the U.S. Department of Energy under Contract Number DE-AC03-76SF00098

DISCLAIMER

LBL-35188
UC-400

Dynamical Behavior of a Premixed Turbulent Open V-Flame

C.W. Rhee,[*‡] L. Talbot,[*‡] J. A. Sethian,[†‡]

[*]Mechanical Engineering Department
University of California

[†]Department of Mathematics
University of California

and

[‡]Lawrence Berkeley Laboratory
University of California
Berkeley, CA 94720 USA

January 1994

This work was supported by the Director, Office of Energy Research, Office of Basic Energy Sciences, Chemical Sciences Division, and Applied Mathematics Subprogram, of the U.S. Department of Energy under Contract No. DE-AC03-76SF00098.

Dynamical Behavior of a Premixed Turbulent Open V-Flame

C.W. RHEE, L. TALBOT*, Mechanical Engineering Department,
and J.A. SETHIAN, Department of Mathematics,
University of California, Berkeley, CA 94720

ABSTRACT. The level set approach of Osher & Sethian to tracking interfaces is successfully adapted to the simulation of a premixed turbulent open V-flame including the effects of exothermicity and baroclinicity. In accord with experimental observations, this algorithm, along with a flame anchoring scheme, predicts flame cusping for a case in which a strong vortex pair interacts with the flame front. The detailed computational velocity and scalar statistics obtained compare well with experimental results by Cheng and Shepherd. Comparison of the conditioned and unconditioned values of these statistics shows that the intermittency factor should be considered for an accurate interpretation of experimental results and better estimation of various theoretical model predictions.

* Author to whom correspondence should be addressed.

1. INTRODUCTION

The propagation of a flame and its interaction with a surrounding turbulent flowfield in a premixed medium is one of the most fundamental and challenging problems of combustion phenomena. The coupling of the chemical reaction with the hydrodynamic flow field makes the problem difficult to analyze, although many models are now available and moderately successful calculations (Ghoniem *et al.*, 1982; Sethian, 1984; Ashurst, 1987) have been conducted. Some models have relied on statistical methods using a probability density function (e.g., Pope, 1976). This pdf is specified empirically or may be derived from an evolution equation which requires certain modeling assumptions. Alternative descriptions have been based on the laminar flamelet concept (Peters, 1986), wherein the flowfield consists of a collection of flame elements embedded in the turbulent stream. The structure of these flamelets (Clavin, 1985) is analyzed separately from the flowfield description so that the complicated chemistry problems are decoupled from the simulation of the turbulent flowfield. In many practical situations, the flame thickness is smaller that the smallest turbulent length scale and flamelet descriptions are relevant.

Here, we simplify one step further beyond the flamelet model and take the zero limit for the flame thickness and solve only for the geometry of the flame front. The flame front acts as an infinitesimally thin boundary which separates regions of constant density and propagates into the fresh mixture at a prescribed flame speed. The speed may be a function of the local curvature of the flame front, which avoids hydrodynamic instability (Darrieus, 1938; Landau, 1944). Fluid elements at the flame front undergo an increase in volume as they burn, creating a jump in the normal component of velocity and a concomitant decrease in density, assuming constancy of pressure across the flame front. This density drop combined with a nonuniform velocity field along the flame creates vorticity and this new vorticity field contributes to the advection of the flame.

Pindera and Talbot (1986, 1988) proposed a computational model for premixed turbulent combustion and showed that production of vorticity at the flame front forms an integral part of the overall velocity field. Their model is based on solving for the turbulent flow field using the discrete vortex method developed by Chorin (1973). The flame front is represented by a set of marker particles. A regridding procedure was employed when marker particles come together in regions where the curvature of the propagating front is large (Hyman, 1984). This regridding procedure resembles diffusion and dominates the actual effects of curvature. In view of the fact that propagating flames can develop cusps, we adopt a level set algorithm, introduced by Osher and Sethian (1988), for following fronts propagating with curvature-dependent speed (Sethian, 1984). The algorithm handles cusping of the flame front naturally and provides an accurate calculation of the curvature which is needed for flame propagation and estimation of flame induced vorticity.

Many experimental studies have been performed to examine the interactions between fluid mechanical turbulence and the combustion process. The open V-flame stabilized by a rod is one of the simple configurations for which various velocity and scalar statistics have been reported (Cheng, 1984; Cheng and Shepherd, 1986; Shepherd *et al.*, 1990). Their results showed that increases in the unconditioned velocity fluctuations and the sharp increase in the Reynolds stress in the flame zone are caused by intermittency contributions associated with the difference in the mean velocities in the reactants and the products regions. They also obtained conditioned velocities and Reynolds stresses in premixed V-flames using a conditional sampling technique to

investigate the true nature of flame-generated turbulence and these conditioned statistics have been used for comparison with numerical results by vortex dynamics models (Pindera and Talbot, 1986) and the BML model (Bray *et al.*, 1977, 1984).

The primary objective of the present study is to adapt the Osher and Sethian level set algorithm to the case of a rod-stabilized premixed V-shaped open flame. To adapt the level set algorithm to this problem, several extensions to the basic numerical schemes are required. They include:

(a) the effect of exothermic volume generation on the flow field, due to the temperature rise across the flame front in the constant pressure flow,

(b) the effect on the flowfield of baroclinic vorticity generation, described by the Hayes (1959) formulation of the vorticity jump condition, thus extending the earlier work of Pindera and Talbot on this effect.

(c) the effect of the free stream turbulence on the flame dynamics, which is modeled by application of Chorin's random vortex technique.

The numerical studies to be described allow the separate evaluation of the importance of each of these effects, and then their combined effect on the overall flame dynamics. The case chosen to be studied in most detail corresponds to the experimental conditions of the investigations by Cheng (1984) and Cheng and Shepherd (1986), and comparisons between their experimental results and the predictions of the present numerical model are presented. A number of detailed computed flowfield properties and turbulence statistical quantities are compared with experimental results. In addition, a separate numerical study is presented describing the interaction of two strong discrete vortices with the flame front and which specifically exhibits the capability of the algorithm to predict the flame cusping phenomena which have been observed experimentally.

In Section 2 we describe the theoretical aspects of our model. Detailed numerical implementation is described in Section 3. We apply the above ideas to a rod-stabilized open V-shaped premixed flame in Section 4. These numerical predictions are compared with experimental results of Cheng and Shepherd in Section 5. We summarize the results in Section 6.

2. PHYSICAL MODEL

In this chapter we present our model for flame propagation and its accompanying flowfield. The main assumptions of the model are:

1) the flow is two dimensional and inviscid,
2) the Mach number is vanishingly small, hence the flow is dynamically incompressible,
3) the flame acts as an interface which separates two regions of different but constant density and propagates into the unburnt gas at a prescribed flame speed S_u which is dependent on the local curvature.

2.1 General Background

Experimental observations on flame propagation have emphasized the importance of the hydrodynamic field associated with the volume expansion due to exothermicity and the vorticity generation due to baroclinicity on the dynamics of combustion. For most flames, the density ratio of reactants to products is five to eight, so the accelerated motion of fluid particles along with vorticity generation plays a significant role in the stability of the flame and may result in distortions of the front which affects the total burning rate.

A common approach to the problem of the interaction between the flow field and the flame consists of separating the fluid dynamic treatment from that of the flame zone by treating the flame front as a surface of discontinuity separating two fluids of different densities. Darrieus (1938) and Landau (1944) found independently that perturbations along a density interface that propagates at a constant speed grow rapidly without bounds and that such flames are absolutely unstable to any perturbation. This is the so-called hydrodynamic instability. Heat conduction improves flame front stability by changing the local value of the burning speed. The concave/convex part of the perturbed flame heats up the reactants more/less than a unperturbed planar flame, thus increasing/decreasing the burning speed. Flames may survive small wavelength perturbations, but long wavelength instabilities persist and have been observed experimentally. Sivashinsky (1977) showed analytically that this instability leads to the formation of a regular cellular structure with a wavelength longer than the flame thickness, and that the nonlinear interaction between the flame front and the flow field leads to a bounded growth of perturbations.

In this work, we model a flame under the stabilizing effects of heat conduction associated with curvature along the flame. Markstein (1964) showed that if the burning speed varies with the curvature of the flame front such that concave/convex flames propagate faster/slower than planar flames, a stabilizing mechanism is realized for short wavelength perturbations, and which is verified experimentally. According to his formulation, the laminar burning speed is given by

$$S_u = S_u^0 \left(1 - \frac{L}{R_f}\right) = S_u^0 \left(1 - L\kappa\right), \tag{2.1}$$

where S_u^0 is the laminar burning speed of a planar flame, often denoted in the literature as S_L, κ is the curvature of the flame front, $R_f = 1/\kappa$ is the radius of curvature of the front and L is the Markstein length scale. The length L is proportional to the laminar flame thickness. An expression for L was deduced by Garcia-Ybarra, Nicoli and Clavin (1984) using high activation energy asymptotics.

2.2 Flowfield Description

In the laminar flame sheet model used here, the flame is considered as a hydrodynamic discontinuity separating reactants and products. Fluid particles experience a sudden drop in density as they burn, creating a jump in the normal component of velocity across the flame front. The discontinuity in density combined with the nonuniform flowfield ahead of the flame creates vorticity in the burnt region. The velocity field due to volume expansion along with the vorticity generation contributes to the new velocity field and to the advection of the propagating flame.

As was done by Pindera and Talbot (1986), we decompose the velocity field **U** into three components:

$$\mathbf{U} = \mathbf{U}_s + \mathbf{U}_v + \mathbf{U}_p, \tag{2.2}$$

with the individual components satisfying the following conditions:

$$\nabla \cdot \mathbf{U}_s = m\,\delta(\mathbf{x} - \mathbf{x}_f)\,;\ \nabla \times \mathbf{U}_s = 0,$$
$$\nabla \times \mathbf{U}_v = \omega(\mathbf{x})\,;\ \nabla \cdot \mathbf{U}_v = 0,$$
$$\mathbf{U}_p = \nabla\phi\,;\ \nabla \cdot \mathbf{U}_p = 0,$$

where $\mathbf{U} = (U,V)$ is the velocity, $\mathbf{U}_s$ the velocity field due to volume expansion across the flame front, $\mathbf{U}_v$ the rotational velocity field due to vorticity, $\mathbf{U}_p$ the potential velocity field, m the volume source strength, $\mathbf{x}_f$ the coordinate describing the position vector of the flame front, $\omega(\mathbf{x})$ the vorticity field, ϕ the velocity potential of the incident flow, $\delta(\cdot)$ is the two-dimensional Dirac delta function, and m is the volume source strength per unit length of the flame.

We derive an expression for the effect of volume expansion on the velocity field, $\mathbf{U}_s$, using the conservation of mass. Let S_u and S_b be the relative normal fluid velocities with respect to the flame on the unburnt and burnt sides, respectively, and let ρ_u and ρ_b be the fluid densities of the unburnt and burnt mixtures. Mass continuity yields

$$\rho_u S_u = \rho_b S_b\,. \tag{2.3}$$

As the reactant converts into the product, volume is generated in this expansion process which is equal to

$$(S_b - S_u) = \left(\frac{\rho_u - \rho_b}{\rho_b}\right) S_u \equiv m\,, \tag{2.4}$$

where S_u is the specified flame speed.

The vorticity transport equation is

$$\frac{D}{Dt}\left(\frac{\omega}{\rho}\right) = \frac{\omega}{\rho}\nabla\cdot U + \nu\nabla^2\omega + \frac{1}{\rho^2}\nabla\rho\times\nabla P, \tag{2.5}$$

The last term on the right of (2.5) is known as the baroclinic torque term and is a source of vorticity through the interaction of gradients of density and pressure. Pressure gradients tangential to the flame will cause different accelerations in the light and heavy gases and hence vorticity will be produced at the flame by the mean density gradient across the flame and the pressure gradient tangential to the flame. It should be noted that although the baroclinic torque term involves the pressure gradient tangential to the flame, pressure gradient effects are of second order as regards to the flowfield due to volumetric sources, and are neglected in the solution of the Poisson equation governing the velocity potential associated with the volumetric sources and the irrotational flowfield.

Hayes (1959) derived a vorticity production equation in the inviscid limit that involves quantities which are continuous across the flame or which have known jump conditions, and Lagrangian time derivatives of quantities in the tangential direction of the interface. According to his formulation, the vorticity jump $[\omega]$ across the flame is expressed as

$$[\omega] = \left(\frac{1}{\rho_b} - \frac{1}{\rho_u}\right)\nabla_s(\rho_u S_u) - \frac{\rho_b-\rho_u}{\rho_u S_u}\left\{\frac{dU_s}{dt} + U_s(\nabla_s U_s - V_n\kappa) - V_n\frac{\partial V_n}{\partial s}\right\}, \tag{2.6}$$

where here U_s is the flow velocity at the flame in the tangential direction, ∇_s its gradient along the flame, and V_n the absolute normal flame speed. $\frac{d}{dt}$ denotes the time derivative taken at a point which always lies on the front and which moves in a direction normal to the discontinuity when it moves. Figure 2.2 shows a sketch of the normal and tangential directions denoted by the subscripts n and s. Defining the stretch K as

$$K \equiv \frac{1}{A}\frac{dA}{dt} = \nabla_s U_s - V_n\kappa,$$

where A is an elemental flame front area, we have

$$[\omega] = \left(\frac{1}{\rho_b} - \frac{1}{\rho_u}\right)\nabla_s(\rho_u S_u) - \frac{\rho_b-\rho_u}{\rho_u S_u}\left\{\frac{dU_s}{dt} + U_s K - V_n\frac{\partial V_n}{\partial s}\right\}. \tag{2.6a}$$

The unsteady term, $\frac{dU_s}{dt}$, was not included in the analysis of Pindera and Talbot.

2.3 Equations for Flame Propagation

It is convenient to formulate the flame propagation problem in terms of an equation for a scalar field $\Psi(x,y,t)$ which describes the flame location. Following Osher and Sethian (1988), we define a continuous initial distance function $\Psi(x,y,t)$ such that $\Psi>0$ in the unburnt region, $\Psi<0$ in the burnt region and the zero-level surface $\Psi = 0$ represents a flame front configuration as is depicted in Fig. 2.2.

To find an equation for the evolution of Ψ which corresponds to the propagating flame, consider the motion of some level set $\Psi(x, t) = C$. Let $x(t)$ be the trajectory of a particle located

on this level set, so

$$\Psi(x(t), t) = C \tag{2.7}$$

The particle speed $\frac{\partial x}{\partial t}$ in the direction n normal to the flame is given by the flame speed $S_u(\kappa)$. Thus,

$$\frac{\partial x}{\partial t} \cdot = S_u(\kappa) \tag{2.8}$$

where the normal vector n is given by $n = \frac{\nabla \Psi}{|\nabla \Psi|}$. By the chain rule,

$$\Psi_t + \frac{\partial x}{\partial t} \cdot \nabla \Psi = 0 \tag{2.9}$$

and substitution yields

$$\Psi_t + S_u(\kappa) \, |\nabla \Psi| = 0 \tag{2.10}$$

2.4 Flame Propagation with Advection

A flame propagates itself with its own burning speed $S_u(\kappa)$ and is also advected by the accompanying flow field. The flame front affects the flow field by volume generation and vorticity production and this flow field influences the flame location by advection. Hence there is a mutual interaction between flame and flow field. In this case the field equation becomes

$$\Psi_t + S_u(\kappa) |\nabla \Psi| + \mathbf{U} \cdot \nabla \Psi = 0. \tag{2.11}$$

The second term represents propagation and the third term denotes advection of the scalar field Ψ.

3. NUMERICAL METHODS

In this chapter, we present the numerical details for an approximation to the equation of motion. To determine the flame motion, a numerical scheme which incorporates the effects of flame propagation, exothermicity and baroclinicity in the level set algorithm is described. The algorithm we employ uses the method of fractional steps to decompose the motion into propagation and advection. First we propagate the flame due to burning. Then we locate the volume sources due to exothermicity and the flame-induced vortices due to baroclinicity to obtain the velocity field for the advection part. A numerical scheme for the flameholder is developed to stabilize the flame against blowout.

3.1 Flame Propagation with Advection

We begin by briefly reviewing the level set approach to tracking propagation interfaces. Complete details may be found in Osher&Sethian (1988), and Sethian (1989).

As shown above, the equation of motion for the propagating interface without advection is given by

$$\Psi_t + S_u(\kappa) \, |\nabla \Psi| = 0 \tag{3.1}$$

where κ is the curvature of the front. We refer to this equation as a "Hamilton-Jacobi" level set formulation. Strictly speaking, it is only a Hamilton-Jacobi equation in the case when S_u is constant, but the flavor of Hamilton-Jacobi equations is present.

This yields an equation of motion for a higher dimensional function Ψ for which a particular level set always corresponds to the motion of the original front. Another way to say this is that we have transformed the Lagrangian equation which would have resulted from a parameterization of the moving interface into an Eulerian equation on a fixed grid of one higher dimension. Thus, if the interface is an $n-1$ dimensional hypersurface, we have traded it in for an n dimensional problem.

Fortunately, the advantages of this exchange far outweigh the additional computational energy required by the extra dimension. To begin, we observe that the function $\Psi(x,t)$ always remains a function, even if the level surface $\Psi = 0$ corresponding to the front changes topology, breaks, or merges. In such cases, parameterizations of the front often break down. As an example, consider two circles in R^2 expanding outwards with normal velocity $V_n = 1$. The initial function Ψ is doublehumped. As Ψ evolves under the Hamilton-Jacobi equation of motion, the topology of the front $\Psi = 0$ changes. When the two circles expand, they meet and merge into a single closed curve with two corners. This is reflected in the change of topology of the level set $\Psi = 0$.

Thus, the level set approach avoids the complex bookkeeping that plagues discrete parameterization techniques when the interface changes topology. Another advantage is that the technique is applicable in any number of space dimensions; calculations of interfaces propagating in three space dimensions are discussed in detail in Osher&Sethian and Chopp&Sethian (1993).

Finally, a crucial advantage of this approach is that, because we have posed an Eulerian problem for the motion of the propagating interfaces, fixed grid finite differences may be used to approximate the equations of motion. While care must be taken to choose difference schemes that satisfy an entropy condition for propagating fronts, the most basic versions of the schemes presented in Osher&Sethian are extremely straightforward and simple to program.

It is tempting to use a central difference approximation to the gradient in the above equation and thus produce the obvious explicit scheme (central difference in space, forward difference in time) for the update Ψ^{n+1}. Unfortunately, such an approximation is unworkable, for reasons which we now explain. For details, see Sethian (1985), Osher&Sethian (1988) and Sethian (1989).

Consider the simple case of a front propagating with speed function $S_u(\kappa) = 1-\varepsilon\kappa$, where ε is a small parameter. The equation of motion for the propagating function Ψ is then given by (see Osher&Sethian),

$$\Psi_t + |\nabla\Psi| = \varepsilon \nabla \cdot \left\{ \frac{-\nabla\Psi}{|\nabla\Psi|} \right\}$$

where here we have used the coordinate-free definition of the curvature. Numerical evidence in Sethian (1985), followed by a proof in Osher&Sethian show that for $\varepsilon>0$, the right-hand-side diffuses sharp gradients and forces the Ψ to stay smooth for all time. Conversely, for $\Psi = 0$, corners develop, and a singularity develops in the curvature. This situation is analogous to solutions of hyperbolic conservation laws, in which the absence of viscosity on the right-hand-side allows the development of shock discontinuities in the propagating solution. Indeed, an entropy condition is required to force the correct solution for propagating interfaces which is equivalent to the one required for hyperbolic conservation laws. A full description of this entropy condition and the parallel between propagating interfaces and hyperbolic conservation laws is given in Sethian,(1989).

Thus, an accurate numerical approximation to the equation for a propagating interface must pick out the correct entropy-satisfying solution and avoid excessive smearing at sharp discontinuities. This leads quite naturally to the use of schemes borrowed from the numerical solutions of hyperbolic conservation laws, where stable, consistent, entropy-satisfying schemes have a rich history.

Complete explanation of the use of shock schemes for approximation the level set equation may be found in Osher&Sethian. Briefly, consider a one-dimensional version of the level set equation for a front advancing with unit speed, and define $H(\Psi_x) = (\Psi_x^2)^{1/2}$. Then a forward time-discrete version of the equation may be written as

$$\Psi^{n+1} = \Psi^n - \Delta t\, H(\Psi_x) \tag{3.2}$$

Let g be an appropriate numerical flux function approximating H. Then we may directly approximates the spatial term and write.

$$\Psi^{n+1} = \Psi^n + \Delta t\, g(D_x^- \Psi_i, D_x^+ \Psi_i) \tag{3.3}$$

where D_x^+ (D_x^-) is the forwards (backwards) difference operator. In multiple space dimensions and the special case where $H(u) = u^2$, a particularly straightforward numerical flux function was given in Osher&Sethian, namely

$$\Psi_i^{n+1} = \Psi_i^n + \Delta t \left\{ \min(D_x^- \Psi_i, 0))^2 + \min(D_x^+ \Psi_i, 0))^2) \right\} \tag{3.4}$$

This conservative monotone scheme is an *upwind* method, in that it differences in the direction of propagating characteristics. Equation (3.4) completely specifies the numerical approximation

to Equation (3.1). Details may be found in Osher&Sethian, and Sethian(1989).

Addition of the curvature correction term to the flame speed $S_u(\kappa) = S_u^o + S_u^1(\kappa)$ requires the separation of the two effects. We approximate the advection part S_u^o with upwind differences as in the above, and the parabolic curvature term $S_u^1(\kappa)$ using central differences. Note that the curvature term κ may be easily computed in this level set setting by observing that the curvature is the divergence of the unit normal, and hence

$$\kappa = \frac{\Psi_{xx}\Psi_y^2 - \Psi_x\Psi_y\Psi_{xy} + \Psi_{yy}\Psi_x^2}{(\Psi_x^2 + \Psi_y^2)^{3/2}} \tag{3.5}$$

The above derivatives are easily approximated using central differences.

Using this approach, a variety of interface problems have been computed in recent years, including problems in mean curvature flow (Chopp&Sethian,1993), flame propagation (Zhu&Sethian,1992) crystal growth and dendritic solidification (Sethian&Strain,1992), compressible gas dynamics (Mulder,Osher&Sethian,1991), minimal surfaces (Chopp,1993), and medical imaging (Malladi,Venuti&Sethian,1993). Some theoretical analysis has been provided in Evans&Spruck (1991).

3.2 Velocity Field due to Exothermicity

At each time step, Ψ is updated to new values on an Eulerian grid by propagation and advection. A new flame position is obtained by passing field data Ψ_{ij} to a contouring routine and finding a set of flame segments corresponding to the level set $\Psi = 0$. The contouring routine works as follows. We locate the cell with four grid values of different signs, then we bisect the cell by the line separating burnt from unburnt region. The position and length of each flame segment within the cell determines the strength of the volumetric source, m, which is given by

$$m = \left(\frac{\rho_u - \rho_b}{\rho_b}\right) S_u \, \Delta l \,, \tag{3.6}$$

where Δl is the elemental flame length. This volume source strength becomes the source term in Poisson equation for the velocity potential computed on an Eulerian grid:

$$\nabla^2 \Phi_{ij} = f_{ij}, \tag{3.7}$$

where Φ is the velocity potential due to volume sources and f is the source strength. In order to use the Poisson solver, the volume source of strength m located in the middle of the flame segment within a cell must be distributed to the four nearest grid points with values f_{ij} using an area weighting scheme.

The computational domain is a rectangle with no-flow boundary conditions across $y = 0, 1$, and inflow-outflow conditions at $x = 0, 2$. The flame propagates in the negative x-direction and volume is generated inside the burnt region due to the density drop across the flame front. The boundary conditions for the Poisson equation should conform to the Neumann compatibility condition which requires that the total volume generated inside the computational domain matches the net outflow across the boundaries of the domain.

Depending on the boundary conditions prescribed, this expansion velocity field affects either both the incoming and outgoing flows or one of them. Since we want the incoming flow

sufficiently far from the flame front to remain intact, the boundary condition is set such that the additional volume generated inside the domain goes out in the positive x-direction only.

The Poisson equation is solved on a discrete grid using a fast Poisson solver (see Swarztrauber,1974). The corresponding vector velocity field due to volumetric sources, $\mathbf{U}_s$, is computed by central differences on Φ_{ij}. (see Eq. 2.2). The irrotational velocity field on the unburnt side of the flame is used for the vorticity generation in the rotational part of the velocity field.

3.3 Velocity Field due to Baroclinicity

The flame acts as a source of vorticity via the baroclinic torque term in the vorticity equation, as well as a volume source. The vorticity jump $[\omega]$ across the flame front is given by (2.6).

The normal and tangential directions on the flame front are as indicated in Fig. 1 and the corresponding unit normal and tangential vectors are expressed in terms of Ψ by

$$\mathbf{n} = -(\Psi_x, \Psi_y) / |\nabla \Psi|,$$

$$\mathbf{s} = (\Psi_y, -\Psi_x) / |\nabla \Psi|.$$

At the four grid points of the cell containing a flame segment we can compute the normal and tangential velocity components of the composite velocity field $\mathbf{U}$ (see Eq. 2.2)

$$U_n = \mathbf{U} \cdot \mathbf{n} = -(U\Psi_x + V\Psi_y) / |\nabla \Psi|,$$

$$U_s = \mathbf{U} \cdot \mathbf{s} = (U\Psi_y - V\Psi_x) / |\nabla \Psi|.$$

The normal and tangential velocity components at the midpoint of the flame segment within the cell are obtained by bilinear interpolation using the velocities at the four surrounding grid points. The absolute flame speed, V_n, is given by

$$V_n = U_n - S_u(\kappa).$$

Once all the values along the flame front are calculated, the space derivative terms in Eq. (3.9) are approximated in the usual fashion. Special care is required for the time derivative term $\frac{dU_s}{dt}$, defined by

$$\frac{dU_s}{dt} = \frac{\partial U_s}{\partial t} + V_n \frac{\partial U_s}{\partial n}.$$

The values Ψ and $\mathbf{U}$ at time $t - \Delta t$ are used to compute U_s at the midpoint of a flame segment at time $t - \Delta t$. At time t, we obtain U_s and V_n at the midpoint of a flame segment using values of Ψ and $\mathbf{U}$ at time t. The first term on the right hand side of the above equation is computed using the values of U_s at time steps t and $t - \Delta t$. To compute the second term on the right hand side, we trace back the distance of amount $V_n \Delta t$ normal to the flame segment into the unburnt region to get U_s and calculate the spatial derivative.

Flame-induced vortices are injected on the burnt side at each time step such that

$$\omega_b = [\omega].$$

These vortices will occupy an area given by

$$\Delta A = S_u \, \Delta l \, \Delta t \, ,$$

where Δl is the length of the flame segment in a given cell, and the corresponding circulation can be expressed as

$$\Gamma_b = \omega_b \, S_u \, \Delta l \, \Delta t \, ,$$

where S_u is the relative velocity of the unburnt gas with respect to the flame front. This vorticity field located behind the flame on the burnt side becomes the source term in the Poisson equation for the vorticity stream function ψ :

$$\nabla^2 \psi_{ij} = -\omega_{ij}, \tag{3.9}$$

where the ω_{ij} at the cell corners on an Eulerian grid are evaluated by area weighting the circulation contained within the cell. We use the vortex-in-cell method (Leonard, 1980) to decrease the computation time. As in the case of the velocity potential due to volume sources, the Neumann compatibility condition should be satisfied such that the negative of the total circulation inside the domain is equal to the contour integral of the normal derivative of the vorticity stream function; given the impermeability condition along the boundaries in the y-direction of the computational domain, this normal component of the vorticity-induced velocity along those boundaries is cancelled by solving the Laplace equation $\nabla^2 \Phi_{ij} = 0$ with the boundary condition that the normal derivative of Φ along the impermeable boundaries is equal but opposite in sign to the normal velocity component of the vorticity-induced velocity. Also the Neumann compatibility condition is satisfied by specifying the boundary conditions along the other boundaries such that the resulting contour integral of the normal derivative of the velocity potential Φ along the boundary should be zero, since the source term is zero in this case.

The addition of the two velocity components, one due to the vorticity stream function and the other due to the potential solver to accommodate the impermeability condition, yields the rotational velocity field due to the vorticity field. This rotational velocity combined with the volume source induced irrotational velocity and the uniform incident velocity specify the total velocity which moves the field data by advection.

We have the equation for flame propagation with advection as is given in Eq. (2.11),

$$\Psi_t + S_u(\kappa) |\nabla \Psi| + \mathbf{U} \cdot \nabla \Psi = 0 \, ,$$

where

$$\mathbf{U} = \mathbf{U}_s + \mathbf{U}_v + \mathbf{U}_p.$$

A first order upwind scheme is used for the advection part

$$\mathbf{U} \cdot \nabla \Psi \approx U_i^+ D_-^x \Psi_{ij} + U_i^- D_+^x \Psi_{ij} + V_j^+ D_-^y \Psi_{ij} + V_j^- D_+^y \Psi_{ij} \, .$$

3.4 Flame Anchoring Algorithm

Power-production devices often require that a flame be retained in the system. Gas velocities in combustors usually exceed the laminar flame speed and hence the flames must be stabilized against blowout, a condition at which flames are transported through the exit of the burner

and thus combustion ceases. In order for a point on a flame front to be stationary, the local condition for stabilization of the flame is that the normal velocity of the unburnt gas and the normal flame speed must be equal. This can be enforced by the presence of a so-called retention point (or line) or a small retention region.

Various objects may serve as retention points: a continuous electrical discharge, a heated metal wire, a blunt body (so that hot combustion products lie in the recirculating region behind it), an auxiliary flame, or other means for continuous ignition of the fresh mixture. The ignition impulse is transmitted from the retention point to neighboring portions of gas at the velocity component of the flow tangent to the flame.

To implement the above idea of flame stabilization into the level set scheme, the flame is attached to the flameholder (or retention point) by laying down an initial ignition field Ψ_{fb} on an Eulerian grid and letting Ψ_{fb} act as a source of an ignition impulse. As the flame propagates and is advected by the accompanying flowfield it is continually reignited at the flameholder by superposing Ψ_{fb} onto the existing Ψ. Further details can be found in Rhee (1992).

We emphasize that our interest in the present work is in the dynamic far-field behavior of open V-shaped flames, and that no attempt is made to model the detailed flowfield structure of any physical flame holder which would be needed to produce such a flame. The flame retention algorithm described is used to ensure that our modeled flames, regardless of their initial assumed shapes, always remain within the computational domain and begin at the retention point (or, more accurately, at the retention cell).

3.5 Some Final Numerical Comments

There are several ways to improve the above algorithm. To begin, the use of a vortex-in-cell method to compute the velocity field from the vortex-vortex interaction means that the vorticity distributions on a scale smaller than the grid size are necessarily lost; this adds numerical smoothing to the flow field which lowers the effective Reynolds number of the computed flow. The representation in the next section of upstream turbulence by means of a distribution of vortex elements of appropriately varying strength is a very simple way to mimic the effects of turbulence; a more accurate way to capture the real statistical flow variations in a turbulent field might come from adjusting both the strengths and the core sizes of the upstream vortex elements. The representation of the flame expansion release on the corners of the grid cell smears somewhat the width of the reaction zone; although as the grid size goes to zero the discretization becomes more accurate. Finally, a more accurate calculation could be performed using more vortex elements by taking advantage of fast N –body solvers, adaptive meshes to track the flame zone more finely, and higher order approximates in the Hamilton-Jacobi level set solvers. Nonetheless, the above algorithm is a good first approximation to the essential physics.

4. RESULTS

The numerical method for flame propagation and flow field description developed above is applied to the dynamic behavior of a V-shaped open premixed flame in an incident turbulent flowfield. Although we are simulating an open flame numerical work requires a finite computational domain. Hence, the solution domain is truncated to a rectangle of axial (x) length equal to 2 and transverse (y) width equal to 1. Incoming fresh mixture enters the computational domain at $x = 0$ with velocity equal to 1. The transverse width which is set to 1 corresponds to the region from $y = 0$ to $y = 1$ in the computation domain. All velocities and lengths are scaled with incoming free stream velocity U_∞ and transverse width respectively; the combination of the two gives a time scale. The flame retention point is located at $(x, y) = (0.5, 0.5)$. Flame speed and density ratio are set to 0.08 and 6.0 respectively, unless otherwise specified. The Markstein length scale in the flame speed equation is set to 0.04 (Garcia-Ybarra, Nicoli and Clavin, 1984). The grid size is equal to 0.02 and the time step is 0.004 which is based on the Courant condition.

Both the kinematic and dynamic responses of the flame are investigated. The kinematic part is simply the case without exothermicity and baroclinicity. The dynamic part is comprised of exothermicity and/or baroclinicity. Also the turbulent flowfield of the incoming flow is simulated by injecting vortices at the domain entrance $x = 0$ whose transverse locations y between 0 and 1 are given in a random fashion. The development of flame cusps in response to a somewhat strong vortex pair is depicted. Various statistical data associated with the turbulence modeling are presented.

4.1 Flame Response without Exothermicity and Baroclinicity

In this case the V-flame simply adjusts kinematically to the incoming flow. The sine of the angle between the flame and the centerline is equal to the laminar flame speed divided by the free stream velocity. Since in the absence of exothermicity the incoming flow is not disturbed by the presence of the flame, the equilibrium shape of the flame should be planar. Figure 2 shows the response of the flame for the flame speed ratio $S_u^\circ/U_\infty = 0.08$. At time $t = 0$, the flame is initialized at an arbitrarily chosen half angle, $\Theta_i = 15^\circ$. The flame closes up at each successive equal time intervals until the equilibrium condition is met. For the case $S_u^\circ = 0.5$ (not shown) the flame when initialized at the same value Θ_i opens up until the equilibrium angle is reached.

4.2 Flame Response with Exothermicity and without Baroclinicity

As the fresh mixture undergoes combustion, volume is generated due to the temperature increase at constant pressure. There are several possible outflow boundary conditions to accommodate this volume production. The Neumann compatibility condition for the Poisson solver requires that the volume generated within the solution domain matches the integral of the net outflow across the boundaries. Since the two side lateral boundaries $y = 0$ and $y = 1$ act as impermeable walls, this generated volume is prescribed along the exit boundary $x = 2$. If the flame does not encompass the whole width of the solution domain, the outflow boundary condition at $x = 2$ can be given in various forms as long as the Neumann compatibility condition is met. Figure 3a show the flame response for the uniform outflow boundary condition at $x = 2$. Compared to the case for the same value of S_u°/U_∞ but without exothermicity, the flame with exothermicity at equilibrium (i.e., after sufficiently many time steps) reaches out to the unburnt

side due to the change of the velocity field in the unburnt side, because the reactants are deflected from the centerline toward the side walls and accelerated in the axial direction. The flame near the flame stabilizer reaches out to the unburnt side and the flame near the exit is mostly convected downstream by the dominant axial flow and hence is positioned almost in line with flow velocity. It is perhaps worth noting here the dangers inherent in attempting to determine experimentally the laminar flame speed S_u^o from the observed flame angle, as has often been done. Without exothermicity, the relationship $\Theta_{eq} = \sin^{-1}(S_u^o/U_\infty)$ holds, but with exothermicity (the physical case) flow divergence and acceleration of the reactants invalidates this relationship, even for an unbounded V-flame (see below). For further discussion on this point, see Cheng *et al.*, (1988).

Figure 3b shows the results for the 'top hat' boundary condition in which the excess volume manifests itself only on the burnt portion at $x = 2$. This boundary condition involves an abrupt jump of velocity across the flame location at $x = 2$. Since the Poisson equation is elliptic, the change in boundary condition is expected to influence the whole solution domain. But compared with case (a) of the uniform exit boundary condition, the flame location and velocity field up to $x = 1.5$ for the two cases are almost identical. From that location on up to the exit, the axial velocity on the unburnt side decelerates and hence the flow diverges towards the centerline to adjust to the 'top hat' boundary condition, causing the contraction of the burnt region of the flame at the exit. This unphysical flame response near the exit is strictly due to the boundary condition. Since our main interest lies away from the exit, the uniform boundary condition will be henceforth employed.

An increased lateral extent of the computational domain would reduce the acceleration of the reactants exterior to the flame, and would also allow increased excursions of the instantaneous flame interface due to turbulence interactions modeled by random discrete vortices, as described later. It would also make more viable a non uniform exit boundary condition, which is more physically realistic then the uniform velocity exit condition employed. However, the acceleration of the reactants exterior to the flame interface is not unphysical. It is observed in experiments, though not as pronounced as is obtained from the computations. At the axial station $x = 1.0$ where we will make our comparisons between computed and experimental results, the experiments show about a 20% increase in reactant axial velocity, whereas the computations yield about a 60% increase. This comparison evidently provides a clue as to the lateral extent of the computational domain required for more faithful modeling, but owing to computational expense, such an inquiry was not pursued.

Although we are simulating an open flame at constant pressure, small pressure gradients in fact are present due to exothermic flow deflection and acceleration, which we neglect except in the calculation of the flame induced vorticity, since they are of second order as regards the flowfield as a whole. In an open flame at essentially constant pressure, the farfield boundary condition due to volume expansion is determined by Eq. (3.6) summed over the instantaneous total length of the flame. The boundary conditions along the truncated domain of the numerical simulation are such that the volume generated due to exothermicity is prescribed at the exit ($x = 2$) and the impermeability condition is imposed at the lateral boundaries ($y = 0$) and ($y = 1$), similar to the flow in a channel. In this confined computational domain, overall mass conservation would require that the mass flow at the inlet ($x = 0$) be equal to the mass flow at the exit ($x = 2$). However, for the cases considered the computed values of the outflow turned out to be greater by about 15% than the inflow. In view of the fact that we are modeling the farfield boundary condition of an open flame with the boundary conditions described above on a finite domain, the

check on the mass conservation is considered satisfactory.

4.3 Response to Two Strong Vortices

Before addressing the more general question of how our model predicts turbulent V-flame dynamics, including the effects of baroclinicity, it is of interest to analyze one of the constituents of the model, namely the interaction of a single line vortex pair with a flame interface. This problem has been studied experimentally by Namer *et al.*, (1984) and Hertzberg *et al.*, (1984) in the context of a Kármán vortex street interacting with a V-flame, and by Roberts and Driscoll (1991) who investigated the response of a flame sheet to a laminar vortex ring. The latter work was subsequently followed by an extensive parametric numerical study of the interaction process (Wu and Driscoll, 1992) using the SLIC algorithm, although the effects of curvature-dependent flame speed, volume generation and baroclinicity were not incorporated. Here we do not present such a parametric study, but rather just a single example which demonstrates how the level set algorithm naturally reproduces the flame cusping phenomenon which is well-established experimentally.

The test case we have analyzed is the release adjacent to the flame retention point at $x = 0.5$, and $t = 0$ of two line vortices of non-dimensional circulation $\Gamma = \pm 0.2$, the positive vortex being on the right and the negative one on the left. The value $|\Gamma| = 0.2$, with our chosen vortex core radius of 0.02, corresponds to a maximum azimuthal velocity-flame speed ratio $(U_{\theta\,max})/S_u^o$ of 20, which places it according to the parametric study of Wu and Driscoll in the 'severely wrinkled' flame regime.

Figures 4 a-d show the sequence of events as the vortex pair passes through the flame. In (a) the vortex pair is seen to have moved outward from its original release points ($y = 0.44, 0.56$ at $x = 0.5$) as it has been advected by the divergent reactant flowfield, but at the same time necking in the flame interface due to the strong circulation of the vortices. As the vortices pass through the flame in (b), (c) (d), cusps develop, which later smooth out as the vortices traverse the product region behind the flame. The computations include volume production at the flame interface, which is reflected in the fact that the interface is curved, but do not include baroclinic vorticity generation. Other calculations have been carried out which incorporate baroclinicity, but the results are not much different from those presented, since the baroclinic vorticity is considerably weaker than the vorticity associated with the interacting vortex pair.

While this single computation does not provide the extent of information given by the parametric investigation of Wu and Driscoll, it does demonstrate the capability of the level set algorithm to deal effectively with vortex-flame interaction, including exothermicity and curvature-dependent flame speed, which is an essential ingredient in the modeling of the dynamical behavior of turbulent flames.

4.4 The Complete Model Including Exothermicity, Baroclinicity and Free Stream Turbulence

The modeling of the effect of exothermicity on the dynamics of the flame interface has been described in Section 4.2. We now add to our model the additional effects on the flame dynamics of turbulence in the oncoming reactant flow and the effect of baroclinic vorticity generation at the flame interface. Additionally, computations were carried out in which free-stream

turbulence and exothermicity were incorporated, but baroclinicity omitted. In the interest of conciseness these results, although referred to, will not be exhibited. Complete details can be found in Rhee (1992).

To simulate computationally the effect of free stream turbulence, vortices of circulation $\Gamma = \pm 0.01$ are injected at $x = 0$, this value of Γ having been found to yield a free stream turbulence level of about 8%. The transverse (y) locations of the injected vortices are distributed between $y = 0$ and 1 using a random number generator. The same number of positive and negative vortices are injected, so that the total free stream circulation remains zero at all times. The time step interval between successive injections of the vortices is chosen such that the mean transverse and axial distances between adjacent vortices are almost equal, as required for the simulation of isotropic turbulence.

As was described in Section 2, vorticity is produced by baroclinicity at the flame interface. The density drop across the flame combined with the tangential pressure gradient along the flame results in predominantly negative (clockwise) flame vorticity behind the right (lower) sheet of the flame and positive (counterclockwise) vorticity behind the left (upper) sheet. When this baroclinic vorticity is combined with the vorticity associated with the modeled free stream turbulence and the flowfield due to the exothermicity, we obtain the flowfield of the complete model.

To model the flame-generated vorticity, the formulation by Hayes which is comprised of steady and unsteady terms is used to give the strengths of the vortices. Since the unsteady term, which was omitted in the simulation by Pindera and Talbot, is calculated to be of the same order of magnitude as the steady terms, both are included in the computation. The baroclinic vortices are at each time step injected on the burnt side of the flame. They are advected by the local flowfield and modify the flame motion and the velocity fields of both reactants and products.

In making comparisons between computed and experimental results, it is desirable to discriminate between passages of unburnt and burnt fluid at a point by means of conditional sampling. To this end, we define an instantaneous progress variable c (x,t) such that c is zero in the reactants and unity in the products. While in the limit of a vanishingly thin flame interface, c can have only 0, 1 values, its mean value $\langle c(x) \rangle$ can range between zero and unity, depending on the fraction of time the observation point is occupied by either reactants or products. This mean value, also termed the intermittency factor, which in the computations is obtained by sampling the time record of a variable and evaluating N_p/N where N_p is the number of samples associated with product fluid and N the total number of samples, forms the basis for conditional sampling. For example, the unconditional Eulerian mean axial velocity at a point is given by

$$U = (1 - \langle c(x) \rangle)\, U_r + \langle c(x) \rangle\, U_p$$

where U_r and U_p are reactant and product axial velocities respectively.

Figure 5 shows the superposition of instantaneous flame shapes at successive time intervals. The brushlike structure of the flame region is evident. The individual flames were found to be generally smooth, with cusping rarely observed. Flame excursions were somewhat greater than what was found in computations in which baroclinic vorticity production was omitted, but the flame shapes were similar.

The velocity field and vortex distribution of one instantaneous flame at $t = 1.4$ are shown in Fig. 6. One can observe from the velocity field, Fig. 6a, that there is an axial acceleration of the flow in both the reactants and the products and that in the products this acceleration is most

pronounced at the centerline y = 0.5. We will return to this point later. Figure 6b shows the distribution of both incident and flame generated vortices within the flowfield for this instantaneous flame. Vortices of positive and negative circulations are represented by filled and open circles, respectively. About 8500 flame-induced vortices are present at this time step, (and a comparable number in the oncoming flow) so for plotting purposes they are combined on an Eulerian grid. Of most interest is the predominance of negative vorticity in the products behind the right (lower) flame sheet, and of positive vorticity behind the left (upper) sheet, as is required from the sign of the baroclinic term $(\frac{1}{\rho^2})\nabla\rho \times \nabla P$. The majority of the vortices in the product region are baroclinic, as computations show that when baroclinicity is omitted the vorticity concentration in the products associated with passage of free stream vortices through the flame is reduced due to the dilatation of the flow.

Figure 7 exhibits the distributions of the unconditioned U_{rms} and V_{rms} just ahead of the flameholder at x = 0.25. (In this and subsequent plots data points are shown only at every third gridpoint, to simplify the plotting). It can be seen that the free streams 'turbulence' is reasonably isotropic, with an intensity of about 8%. V_{rms} of course goes to zero at y = 0, 1, because of the sidewall impermeability boundary condition. Figure 8 shows for comparison the distribution of these quantities at x = 1.0, behind the flameholder. An overall increase in the turbulence level can be seen. This increase, in the burnt region, is due mainly to the baroclinic vortices, as was determined by comparison with the results obtained when baroclinicity was omitted. The conditioned values of U_{rms} at x = 1.0, shown in Figure 9, are found to be not significantly different from the unconditioned values. However, the conditioned values of V_{rms} (not shown), while on average are about the same as the unconditioned values, do not exhibit the peaks at the flame brush, y = 0.3 and 0.7, of the latter. These peaks are evidently due to flame intermittency.

Unconditioned average axial velocity distributions at x = 0.25 and x = 1.0 are shown in Figure 10. The acceleration of the flow in the products near the centerline is evident. This acceleration is a baroclinic effect, since it was not observed in the absence of flame-generated vortices. The conditioned average transverse velocity at x = 1.0 is shown in Figure 11. As seen, the mean V velocity is away from the flame in the reactants, and towards the centerline in the products, due to the reversal of flow direction across the flame brush.

Values of unconditioned and conditioned kinematic Reynolds stress $-\overline{uv}$ are plotted in Figures 12 and 13. While the distributions are somewhat noisy, one feature of interest is that the reversal spikes at the flame location y = 0.3, 0.7 present in the unconditioned data are absent in the conditioned data. This again is an intermittency effect. Notice also that the Reynolds stress is clearly positive on the left hand side and negative on the right hand side within the products. This is a manifestation of the predominance of positive and negative flame generated vorticity in the products on the left and right hand sides respectively, since the U fluctuations have no preferred sign. It is also interesting that near the location of the flame brush the Reynolds stresses in the reactants and in the products are of comparable magnitudes.

The probability distribution of values of flame curvature is shown in Figure 14. The average value is near zero and there is a small negative skewness. The flame brush thickness along the flame is plotted in Figure 15. Compared to results without baroclinicity, the flame brush thickness is found to have a slight increase. (The reduction in apparent flame thickness near the exit is an artifact of the sidewall and outflow boundary conditions). The disturbances in the flame configuration near the flame holder are affected by the flame vortices and this augments the flame wriggles and the thickening of the flame brush. The probability distributions of flame

crossings for reactants and products between the instantaneous flame and the average flame location $\langle c \rangle = 0.5$, are shown in Figure 16. The resulting probability distributions when baroclinicity is omitted are about the same.

The spatial velocity correlation function can be calculated if simultaneous records are obtained at two spatially separated points, from the integral

$$R_{uu}(r) = \frac{1}{\langle u^2 \rangle T} \int_{t_0}^{t_0+T} u(y_0,t)\, u(y_0+r,t)\, dt.$$

The construction of a curve of the correlation R_{uu} requires a lot of measurements of the velocity fluctuation u, since the integral has to be repeated for enough values of the spatial separation r and the sampling time T to define the curve. A whole family of such curves can be produced by varying the direction of the line connecting the two observation points. The integral length scale l_y is obtained as the definite integral over r of the correlation R_{uu}, with r taken in the y-direction. In the calculation of the integral length scale, the fixed point y_0 is located at the centerline $y = 0.5$ and the separation r varies from the centerline to the lateral boundary with spacing 0.02. The reactant length scale was computed at $x = 0.25$, and the product length scale at $x = 1.0$. The values obtained were $l_y = .0248$ and 0.0660, respectively, in normalized units. The increase in l_y in the products is due to volumetric expansion, as would be expected on physical grounds.

5. DISCUSSION AND COMPARISON WITH EXPERIMENT

In a typical experimental premixed turbulent V-flame configuration (Cheng, 1984; Cheng and Shepherd, 1984; Cheng *et al.*, 1988) which is suitable for comparison with this numerical simulation, an inner core of fuel/air mixture 5.0 cm in diameter is surrounded by an outer co-flow of air to reduce shear layer effects in the reactants. The turbulent flame is stabilized by a 1.0 mm diameter rod placed at the exit of the flow nozzle. The incident freestream turbulence is generated by a square mesh grid or a perforated plate. The freestream velocity is about 5 m/s, the turbulence level is between 5 and 8 percent of the free stream and the laminar flame speed is 40 to 50 cm/s. Flame statistics such as turbulence intensity, Reynolds stress, length scales, flame brush thickness are reported, and provide the means for direct comparison with the present numerical simulation.

The values of S_u^o and the strength, number and frequency of injected vortices for the numerical simulation of the incident flow turbulence level were specifically chosen with the intention to compare with the above experimental results. The computational results we present have some features in common with the results obtained by Pindera and Talbot and Ashurst (1987) on a V-flame using a Lagrangian vortex method. These authors employed a Lagrangian method for flame propagation using marker particles along the flame location. The volume sources used in their simulations to accomplish the velocity field due to combustion affect the velocity field in all directions in contrast with the present work in which the volume sources are unidirectional. Also, the flame induced vorticity due only to steady terms was included in the simulation by Pindera and Talbot, and baroclinicity was not included in Ashurst's work.

Since we are simulating an open flame and do not model the detailed features of the flameholder region, there is no intrinsic length scale present. One way of establishing a scaling relationship is to relate the computed integral length scale to the physical integral length scale. The cold stream integral length scale is calculated to be 1.24 times the grid size. This is a transverse length scale l_y, a two-point quantity. The measured integral scale was obtained to be about 3 mm (Cheng *et al.*, 1988). This is, however, the streamwise length scale, l_x, determined from a single point time series using the Taylor hypothesis which states that the turbulence is convected with negligible change past the measurement point at the average local velocity. Since the free steam turbulence in the numerical simulation was very nearly isotropic, it is assumed that the condition of $l_x = 2\, l_y$ applies, and this allows us to relate the numerical scale of the computations to the physical scale of the experiments. This means that the grid size which has the value 0.02 in the computations corresponds to about 1.2 mm in physical scale. All numerical results can then be converted to the physical scale using this relation for direct comparison with experimental results. Most of statistical data in the product region of this work were obtained at $x = 1.0$ which corresponds to 30 mm downstream of the flameholder in the physical scale and these will be compared with the experimental results reported at the location 50 mm downstream of the flameholder in the work of Cheng (1984).

We first consider the computed flame response to two strong vortices, in comparison with the experimental observations of Herzberg *et al.* (1984) on the interaction of a Kármán vortex street with a V-flame. Flame cusping was observed in the experiment, though not as strong as was obtained in the numerical simulation. The flame configuration produced in the cusping process clearly depends on the ratio of the maximum vortex-induced velocity to the freestream velocity as the vortex interacts with the flame. For a Kármán vortex street at $Re = 240$ of the experimental conditions, this ratio is in the vicinity of 0.3 (Blake, 1986), whereas this value was

about 1.6 in the numerical simulation. This rough estimate suggests that the cusping observed in the experiment might be expected to be less severe than that found in the numerical simulation, although it is clear that they share the same general structure. For the weak incident turbulence level chosen for the complete simulation, essentially no flame cusping was observed.

The mean velocities in the flame region shows that the products move faster than the reactants and that flow direction is towards the centerline for products and is away from the centerline towards the side walls for reactants, which is also observed experimentally. There is a significant increase in the centerline axial velocity due to flame vorticity as compared with the case of exothermicity only, a characteristic of the flowfield clearly evident in the experimental results. This effect was also found by Pindera and Talbot and is a striking feature of the effect of baroclinicity. The conditioned values of U_{rms}, V_{rms} and the Reynolds stress in the burned region with baroclinicity included show an overall increase, compared with exothermicity only. These conditioned data indicate that the flame generated vorticity plays an important part in determining the turbulent flow field. The flame vortices are responsible for the increase in the conditioned turbulent intensities in the products compared to the case without flame generated vortices and are therefore considered to be the true source for the so-called flame generated turbulence since the conditioned results do not include the effects of intermittent flame motions. In the experimental results of Cheng (1984), the conditioned values of U_{rms}, V_{rms} within the flame brush are higher by about two times than those in the reactant region. But these values within the flame brush decay to the level of the values in reactant in the post flame region. Since the turbulence cascade and viscous dissipation are not included in the numerical model, this decay of turbulence level was not observed in the numerical simulation. But we can at least estimate how much the turbulence level decays in the product region. According to the experimental results by Batchelor and Townsend (1948) on the decay of isotropic turbulence in the initial period, about a 50% decay in the turbulence level from $x = 1.0$ to $x = 2.0$ (which is equivalent to 60 mm in distance) is estimated. This suggests that after the turbulence level withing the flame brush region is increased by flame generated vortices, viscous dissipation takes over within the product region to reduce the turbulence level significantly. The kinematic Reynolds stress within the flame brush in the experiment had a maximum absolute value of about 0.08 $(m/s)^2$. The Reynolds stress in the product region is calculated to be about 0.004 which is equal to 0.1 $(m/s)^2$ in physical dimension, in satisfactory agreement with experiment.

The flame brush thickness was calculated to be about 0.15 across the transverse axis at $x = 1.0$, equivalent to 9 mm in physical dimension. This is within the range of experimental values of 4 to 10 mm. In the work of Pindera and Talbot (1986), the flame brush thickness including baroclinicity was found to be slightly smaller than that without baroclilnicity, whereas the opposite is true according to our simulation. While the reason for this is unclear, it may be associated with the neglect by Pindera and Talbot of the unsteady term in the vorticity jump relation, the relatively sparse number of flame vortices (about 400) employed by them as compared with the present computations which involved as many as 8500, and possibly most importantly, the superiority of the level set algorithm over the marker particle method employed by Pindera and Talbot to track the flame motion. A qualitative comparison between a computed flame interface and one observed experimentally is displayed in DOE Lawrence Berkeley Laboratory Report LBL 33445, UC 350, July 1993. The comparison reveals that the experimentally observed flame excursions are considerably greater than those computed, undoubtedly in part because of the constraint of the finite lateral extent of the computational domain, and the rather coarse grid used in the computations. Both of these limitations could be relaxed in future work,

at the expense of increased computational cost.

The distance between flame crossings at maximum probability is found to be about 0.2 which in physical dimension means that the instantaneous flames meet with the average location of the flame at 12 mm intervals at maximum probability. This translates into a mean flame crossing frequency of about 500 Hz whereas the experimental value was found to be about 600 Hz (Cheng *et al.*, 1988), in good agreement.

The probability distribution of curvature along the flame front compares well with experimental results (Shepherd and Ashurst, 1992) although the experiments were done on a stagnation flame. Positive and negative curvatures are about equally present with slight negative skewness for a weakly turbulent flame.

6. CONCLUSIONS

The level set algorithm, with volume generation and flame vorticity included, provides a simulation of turbulent premixed flame dynamics in quite good agreement with experimental results for input parameters chosen to agree with experimental conditions No adjustable parameters other than the Markstein length scale are involved. Some of the important features predicted for the case investigated are:

a) flame brush thickness
b) velocity rms and Reynolds stress levels
c) product axial velocity acceleration
d) flame crossing frequency
e) flame curvature distribution

Flame generated vorticity is found to have an important effect in the prediction of velocity rms values, Reynolds stresses and particularly the axial flow acceleration in the product region behind the flame which is observed experimentally. The unsteady and steady terms in the vorticity jump relationship contribute about equally to the total flame generated vorticity.

The comparisons between conditioned and unconditioned statistics for velocity rms values and Reynolds stresses showed that the intermittency effect plays a major role in the statistics of turbulent premixed flames and therefore requires special attention in theoretical models. The unconditioned (Eulerian) flame statistics can be quite misleading in that these are mainly due to intermittent measurements in the reactants and products. The conditioned (Lagrangian) flame statistics do not show sharp peaks in U_{rms}, V_{rms} and the Reynolds stress within the flame brush such as are found in the unconditioned data. This is also in accord with Cheng's experimental results and suggest that the Eulerian results without knowledge of flame locations lead to erroneous interpretations, and emphasizes the importance of the conditioned velocity statistics for a better understanding of the dynamics of the flame front.

The level set algorithm is shown to predict flame cusping for a situation in which a strong vortex interacts with the flame front, in accord with experimental observations of the passage of a Kármán vortex street through a flame. In addition, for the relatively low turbulence level chosen for the full numerical simulations, cusping was rarely found, and the statistics of flame curvature exhibit essentially a symmetrical distribution about a zero mean, similar to what has been observed experimentally for a stagnation-point flame. Volume generation at the flame front is shown to play a decisive role in determining the flame angle, and it is shown clearly that the experimental evaluation of the "turbulent burning velocity" through observation of the flame angle leads to erroneous result, if the outward deflection and the acceleration of the incoming flow in not taken into account, as has also been established experimentally by Cheng and Shepherd.

REFERENCES

Ashurst, W.T., (1987), *Vortex Simulation of Unsteady Wrinkled Laminar Flames,* Combust. Sci. and Tech., 52, pp. 325-351.

Batchelor, G.K. and Townsend, A.A., (1948), *Decay of Isotropic Turbulence in the Initial Period,* Proc. R. Soc., 1035, pp. 539-558

Blake, W.K., (1986), *Mechanics of Flow-induces Sound and Vibration,* Vol. I, Chap. 5, Academic Press, Inc., New York

Bray, K.N.C., Libby, P.A., and Moss, J.B., (1986), *Flamelet Crossing Frequencies and Mean Reaction Rates in Premixed Turbulent Combustion,* Combust. Sci. and Tech., 41, pp. 143-172

Bray, K.N.C., and Moss, J.B., (1977), *A Unified Statistical Model of the Premixed Turbulent Flame,* Acta Astronautica, 4 pp. 291-319

Cheng, R.K., (1984), *Conditional Sampling of Turbulence Intensities and Reynolds Stress in premixed Turbulent Flames,* Combust. Sci. and Tech., 41, pp. 109-142

Cheng, R.K. and Shepherd, I.G., (1986), *Interpretation of Conditional Statistics in Open Oblique Premixed Turbulent Flames,* Combust. Sci. and Tech., 49, pp. 17-40

Cheng, R.K. and Shepherd, I.G. and Talbot, L., (1988), *Reaction Rates in Premixed Turbulent Flames and Their Relevance to the Turbulent Burning Speed,* Twenty-Second Symposium (Int'l) on Combustion, The Combustion Institute, Pittsburgh, PA, pp. 771-780

Chopp, D., (1993), *Computation of Minimal Surfaces using Level Sets,* to appear, J. Comput. Phys.

Chopp, D., and Sethian, J.A., (1993), *Curvature Flow and Singularity Development,* submitted for publication, J. Exp. Math

Chorin, A.J., (1973), *Numerical Study of Slightly Viscous Flow,* J. Fluid Mech., 57, pp. 1-59

Clavin, P., (1985), *Dynamic Behavior of Premixed Flame Fronts in Laminar and Turbulent Flows,* Energy Combust. Sci., 11, pp. 109-142

Darrieus, G., (1938), Unpublished work, Sixth Int. Congress of Appl. Mech., Paris

Evans, L.C., and Sprunk, J., (1991), *Motion of Level Sets by Mean Curvature, I,* J. Diff. Geom., 33, pp., 635-681

Garcia-Ybarra, P., Nicoli, C. and Clavin, P., (1984), *Soret and Dilution effects on Premixed Flames,* Combust. Sci. and Tech., 42, pp. 87-109

Ghoniem, A.F., Chorin, A.J. and Oppenheim, A.K., (1982), *Numerical Modeling of Turbulent Flow in a Combusion Tunnel,* Phil. Tran. R. Soc. Lond., A304, pp. 303-325

Hayes, W.D., (1959), *The vorticity Jump Across A Gasdynamic Discontinuity,* J. Fluid Mech., 2, pp. 595-600

Hyman, J.A., (1984), *Numerical Methods for Tracking Interfaces,* Physica 12D, pp. 396-407

Hertzberg, J.R., Namazian, M. and Talbot, L., (1984), *A Laser Tomographic Study of a Laminar Flame in a Karman Vortex Street,* Combust. Sci. and Tech., 38, pp. 205-216

Landau, L., (1944), *A Contribution to the Theory of Slow Combusiton,* J. Exp. Theor. Phys., 14, p 240

Leonard, A., (1980), *Vortex Methods for Flow Simulation,* J. Comp. Phys., 37, pp. 289-335

Malladi, R., B. Venuti, and Sethian, J.A., (June 1993), *A Shape Detection Scheme Using Level Sets,* submitted for publication, IEEE Journal on Image Analysis

Markstein, G.H., (1964), *Nonsteady Flame Propagation,* Pergamon Press, Ltd.

Mulder, W., Osher, S.J., and Sethian, J.A., (1991), *Computing Interface Motion: The Rayleigh-Taylor and Kelvin-Helmholtz Instabilities,* to appear, Journal of Computational Physics

Namer, I., Bill, R.G. Jr., Talbot, L. and Robben, F. (1984), *Density Fluctuations in a Karman Vortex Street,* AIAA J. 22, pp. 647-654

Osher, S.J., and Sethian, J.A., (1988), *Fronts Propagating with Curvature-Dependent Speed: Algorithms based on Hamilton-Jacobi Formulations,* J. Comp. Phys., 79, pp. 12-49

Peters, N., (1986), *Laminar Flamelet Concepts in Turbulent Combustion,* Twenty-first Symposium (Int'l) on Combustion, The Combustion Institute, Pittsburgh, PA, pp. 1231-1250

Pindera, M.-Z. and Talbot, L., (1986), *Flame Induced Vorticity: The Effects of Stretch,* Twenty-first Symposium (Int'l) on Combustion, The Combustion Institute, Pittsburgh, PA, pp. 1357-1366

Pindera, M.-Z. and Talbot, L., (1988), *Some Fluid Dynamic Considerations in the Modeling of Flames,* Combustion and Flame, pp. 111-125

Pope, S.B., (1976), *The Probability Approach to the Modeling of Turbulent Reacting Flows,* Combustion and Flame, 27, pp. 299-312

Rhee, C.W. (1992), *Dynamical Behavior of a Premixed Open V-Flame with Exothermicity and Baroclinicity,* Ph.D. Thesis, Mechanical Engineering, University of California, Berkeley.

Roberts, W.L. and Driscoll, J.F. (1991), *A Laminar Vortex Interacting with a Premixed Flame,* Combust. Flame, 87, pp. 245-256

Sethian, J.A., (1984), *Curvature and the Evolution of Fronts,* Commun. Math. Phys., 101, pp. 487-499

Sethian, J.A., (1989), *A Review of Recent Numerical Algorithms for Hypersurfaces Moving with Curvature-Dependent Speed,* J. of Diff. Geom., 31, pp. 131-161

Sethian, J.A., and Strain, J., (1992), *Crystal Growth and Dendrite Formation,* J. Comp. Phys. 98, 2, pp. 231-253

Shepherd, I.G. and Ashurst, W.T., (1992), *Flame Front Geometry in Premixed Turbulent Flames,* Twenty-Fourth Symposium (Int'l) on Combustion, The Combustion Institute, Pittsburgh, PA, pp 485-491

Shepherd, I.G., Cheng, R.K. and Goix, P.J., (1990), *The Spatial Scalar Structure of Premixed Turbulent Stagnation Point Flames,* Twenty-Third Symposisum (Int'l) on Combustion, The Combustion Institute, Pittsburgh, PA, pp. 781-787

Sivashinsky, G.I., (1977), *Nonlinear Analysis of Hydrodynamic Instability in Laminar Flames,* Acta Astronautica, 4, pp. 1177-1207

Swarztrauber, P.N., (1974), *A Direct Method for the Discrete Solution of Separable Elliptic Equaitons,* SIAM J., Numer. Anal., 11, pp. 1136-1150

Wu, M-S and Driscoll, J.F., (1992), *A Numerical Simulaiton of a Vortex Convected Through a Laminar Premixed Flame,* Combust. Flame, 91, pp. 310-322

Zhu, J., and Sethian, J.A., (1992), *Projection Methods Coupled to Level Set Interface Techniques,* J. Comp. Phys., 102, 1, pp. 128-138

ACKNOWLEDGEMENTS

This work was supported by the Director, Office of Energy Research, Office of Basic Energy Sciences, Chemical Sciences Division of the U.S. Department of Energy under Contract No. DE-AC-03-76F00098, with Dr. F. Dee Stevenson as contract monitor. Additional support

was provided by the Applied Mathemetics Subprogram of the Office of Energy Research under Contract No. DE-AC-03-76F00098

The authors would like to thank Dr. Robert Cheng for his valuable discussions and suggestions.

FIGURE CAPTIONS

fig.1 Flame front configuration and nomenclature.

fig.2 Flame response without exothermicity and baroclinicity for $S_u^o/U_\infty = 0.08$. Flame angle is inititalized at half angle $\Theta_i = 15^o$. and reaches the equilibrium angle $\Theta_e = \sin^{-1}(S_u^o/U_\infty)$ after a sufficient number of time steps.

fig.3 Flame response with exothermicity for a density ratio $\rho_u/\rho_b = 6$, and flame speed $S_u^o/U_\infty = 0.08$. Flame initialized at $\Theta_i = 15^o$. (a) Uniform exit velocity boundary condition. (b) 'Top hat' exit velocity boundary condition.

fig.4 Passage of a vortex pair through a flame front.

fig.5 Superposition of instantaneous flame configurations at successive time steps for $\rho_u/\rho_b = 6$, $S_u^o/U_\infty = 0.08$, with baroclinic vorticity production included.

fig.6 An instantaneous flame configuration at t=1.2 for the conditions of Figure 5. (a) Velocity field, (b) vortex distribution; filled symbols - positive circulation, open symbols - negative circulation.

fig.7 Velocity variances U_{rms} and V_{rms} at x = 0.25, ahead of flameholder.

fig.8 Unconditioned velocity variances U_{rms} and V_{rms} at x =1.0, downstream of flame-holder.

fig.9 Conditioned variance U_{rms} at x =1.0, in the reactants (filled symbols) and products (open symbols).

fig.10 Unconditioned average axial velocity U at x = 0.25 (filled symbols) and x = 1.0 (open symbols).

fig.11 Conditioned average transverse velocity V at x = 1.0 in reactants (filled symbols) and products (open symbols).

fig.12 Unconditioned kinematic Reynolds stress at x = 0.25 (filled symbols) and x = 1.0 (open symbols).

fig.13 Conditioned kinematic Reynolds stress at x = 1.0 in reactants (filled symbols) and products (open symbols).

fig.14 Normalized probability distribution function of flamefront curvature.

fig.15 Axial variation of mean flame brush thickness, as defined by the $\langle c \rangle = 0.1$ and $\langle c \rangle = 0.9$ contours.

fig.16 Normalized probability distribution functions of the crossing distances between instantaneous flames and the average flame location $\langle c \rangle = 0.5$ for reactants (filled symbols) and products (open symbols). The similarity of the two pdf's indicates the absence of any significant cusping.

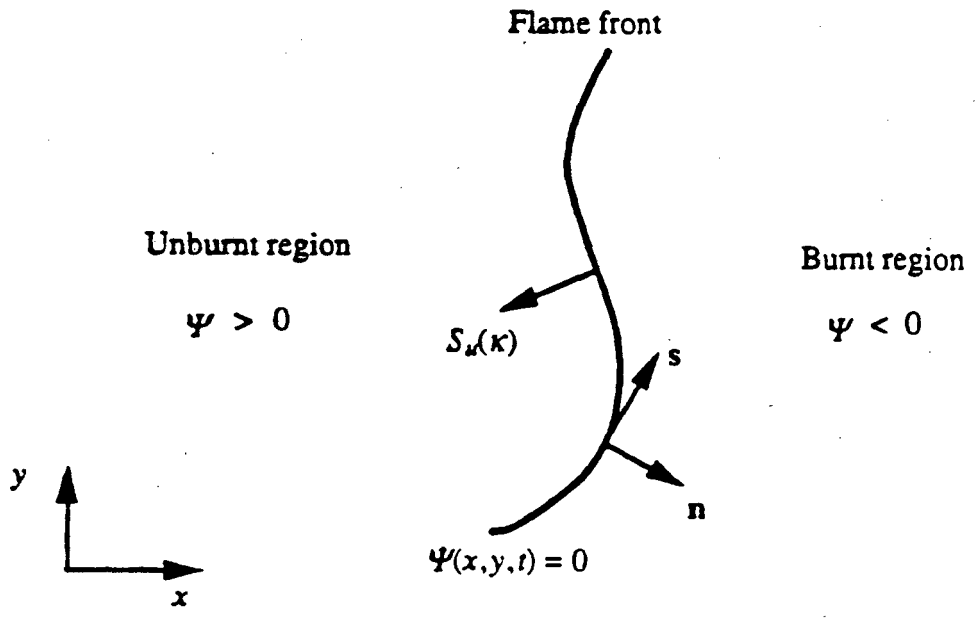

Fig.1 Flame front configuration and nomenclature.

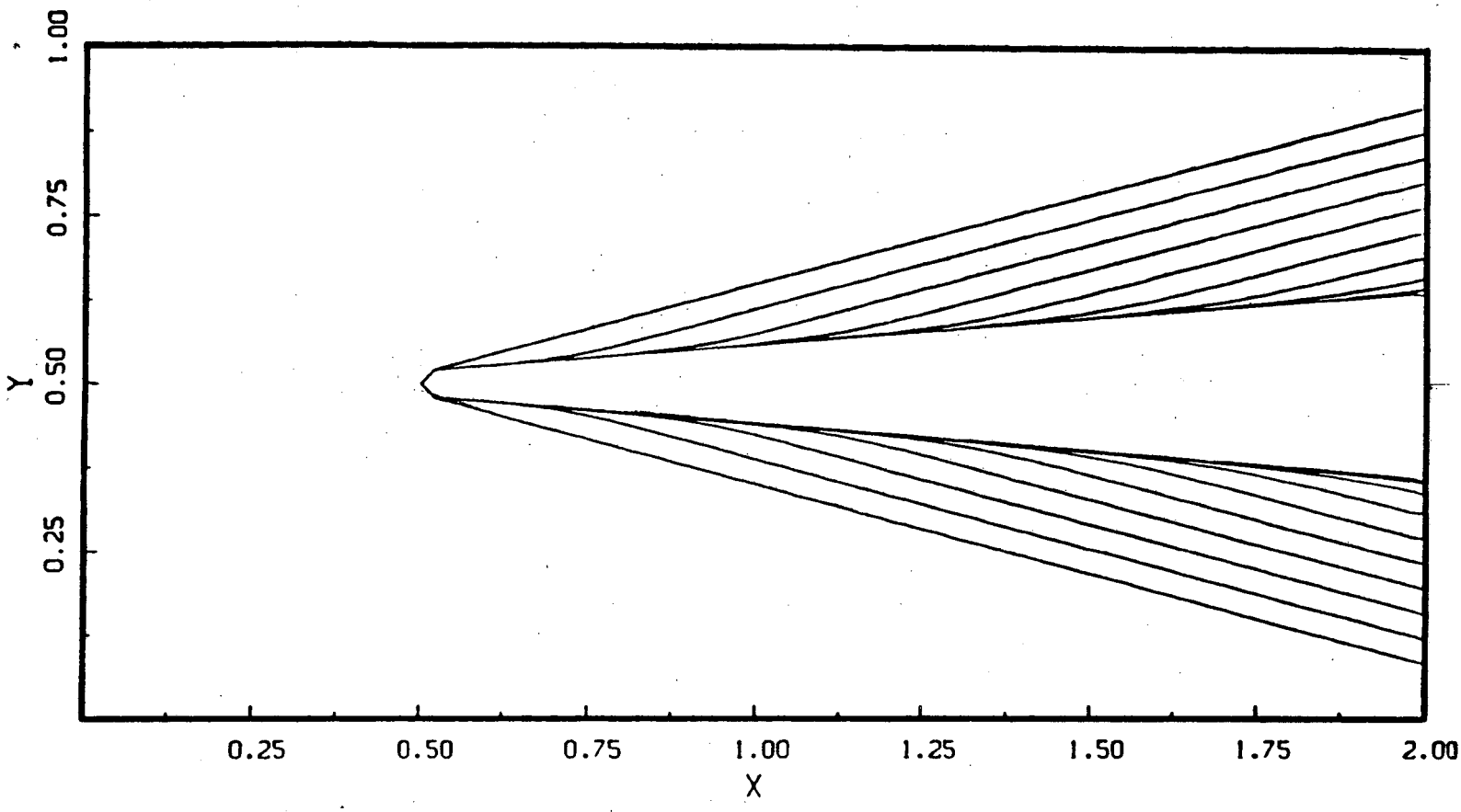

Fig.2 Flame response without exothermicity and baroclinicity for $S_u^\circ/U_\infty = 0.08$. Flame angle is inititalized at half angle $\Theta_i = 15^\circ$. and reaches the equilibrium angle $\Theta_e = \sin^{-1}(S_u^\circ/U_\infty)$ after a sufficient number of time steps.

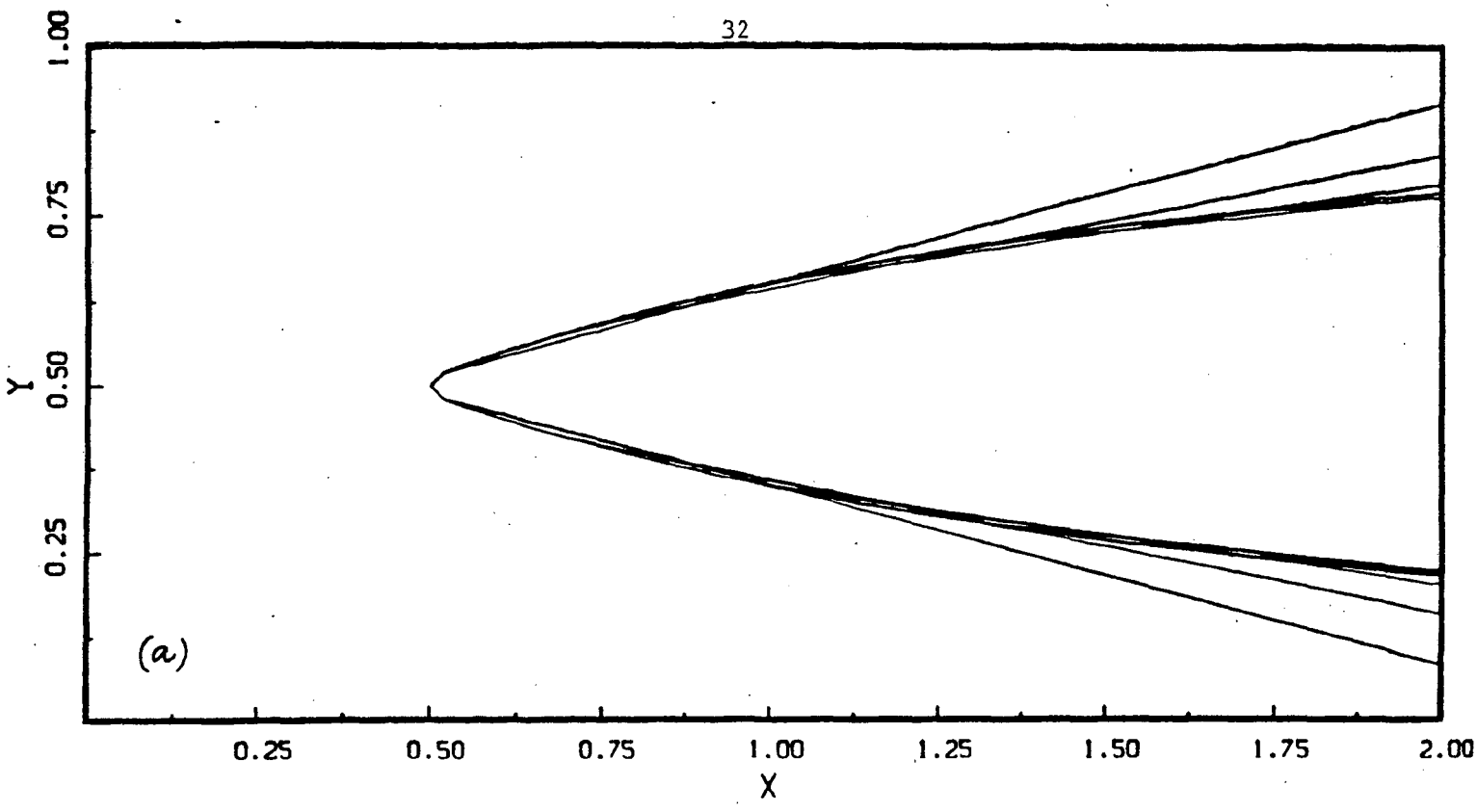

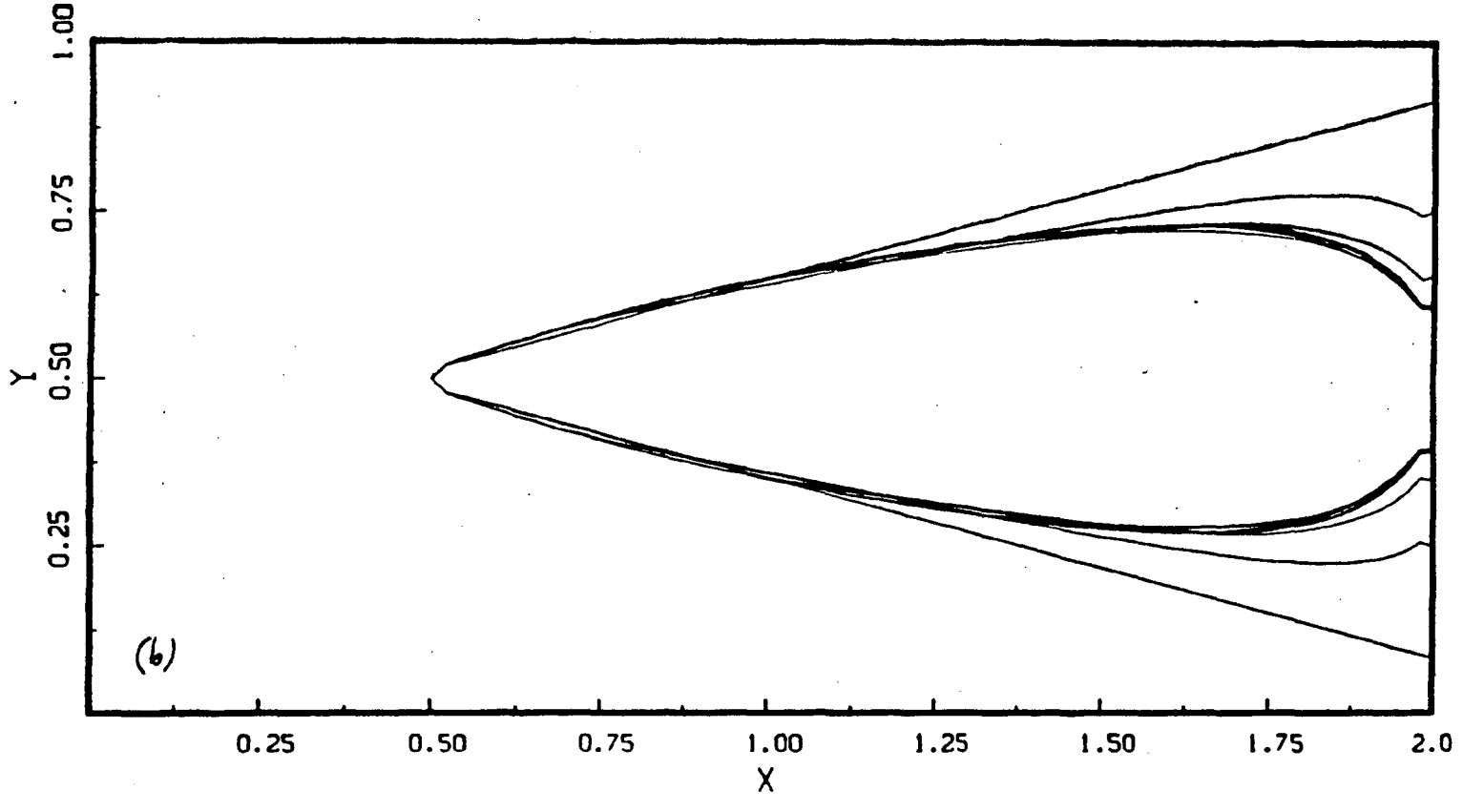

Fig.3 Flame response with exothermicity for a density ratio $\rho_u/\rho_b = 6$, and flame speed $S_u^\circ/U_\infty = 0.08$. Flame initialized at $\Theta_i = 15^\circ$. (a) Uniform exit velocity boundary condition. (b) 'Top hat' exit velocity boundary condition.

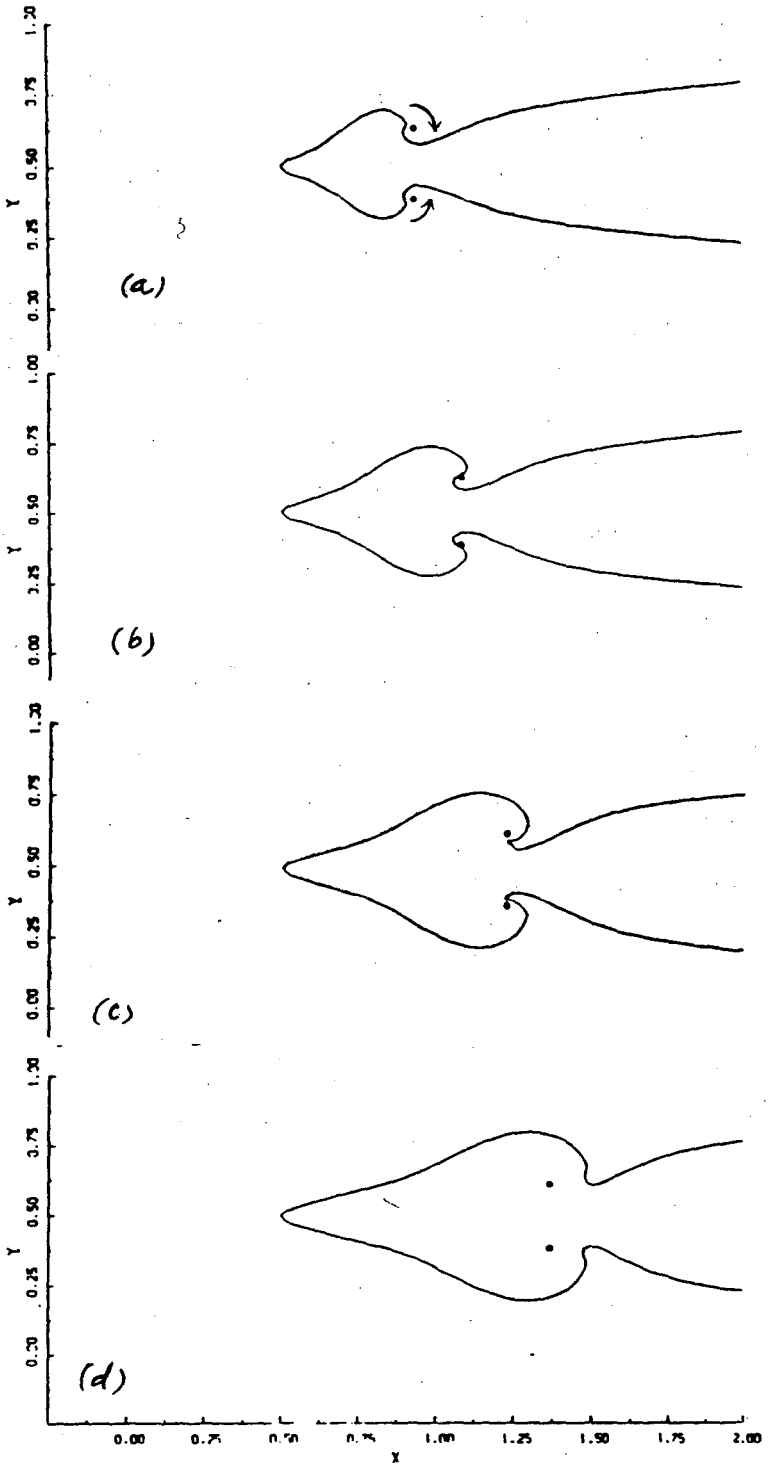

Fig.4 Passage of a vortex pair through a flame front.

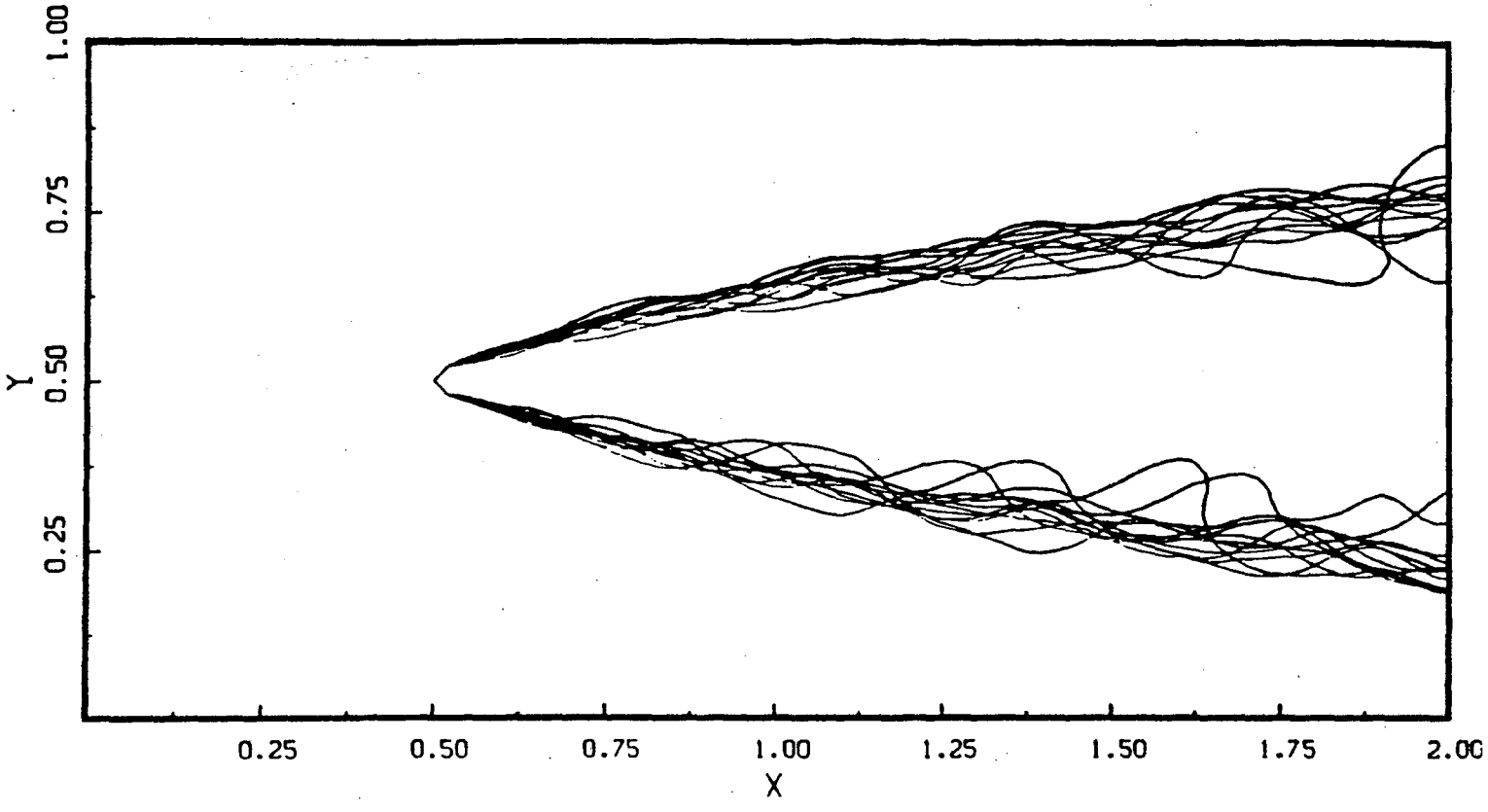

Fig.5 Superposition of instantaneous flame configurations at successive time steps for $\rho_u/\rho_b = 6$, $S_u^o/U_\infty = 0.08$, with baroclinic vorticity production included.

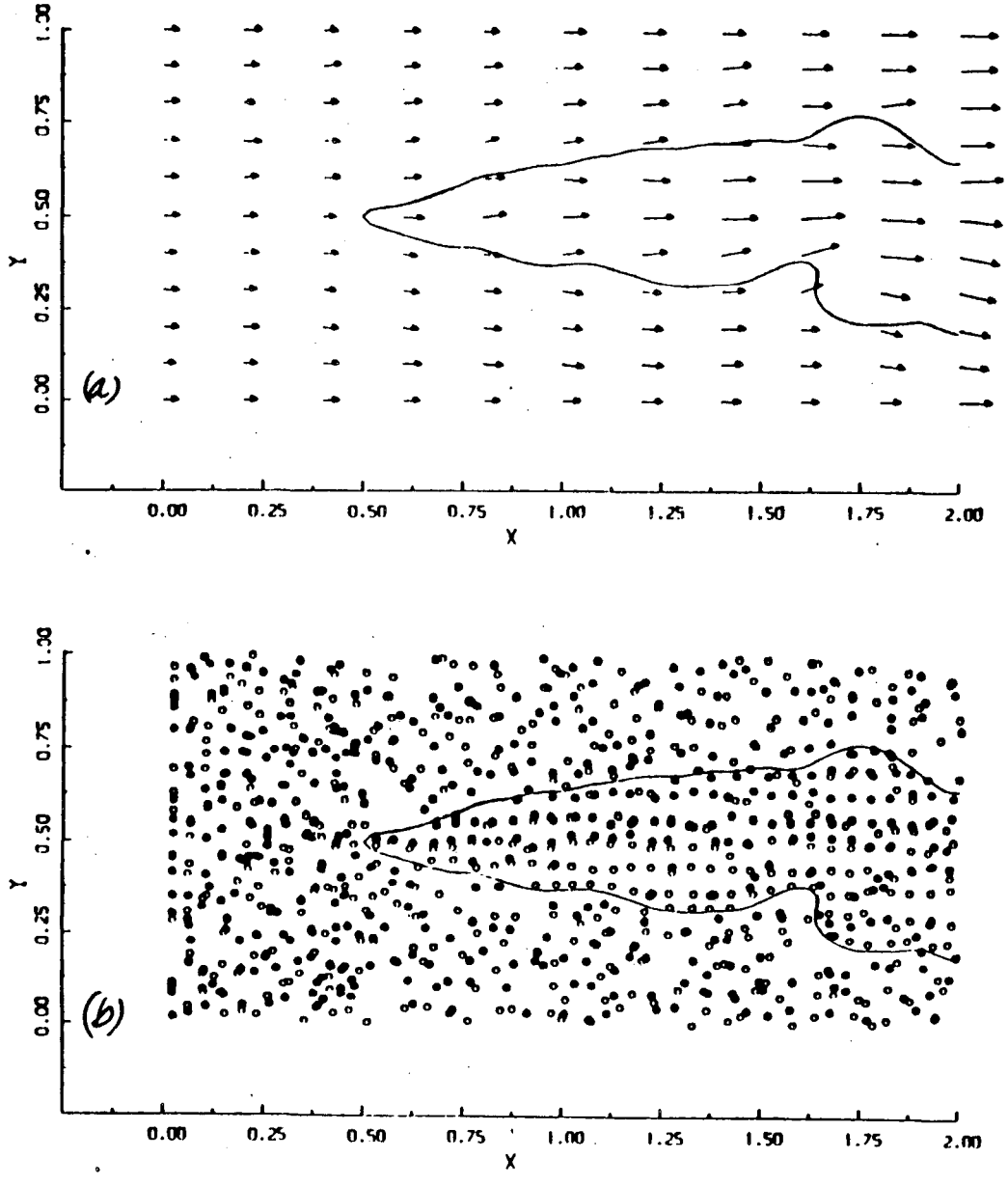

Fig.6 An instantaneous flame configuration at t =1.2 for the conditions of Figure 5. (a) Velocity field, (b) vortex distribution; filled symbols - positive circulation, open symbols - negative circulation.

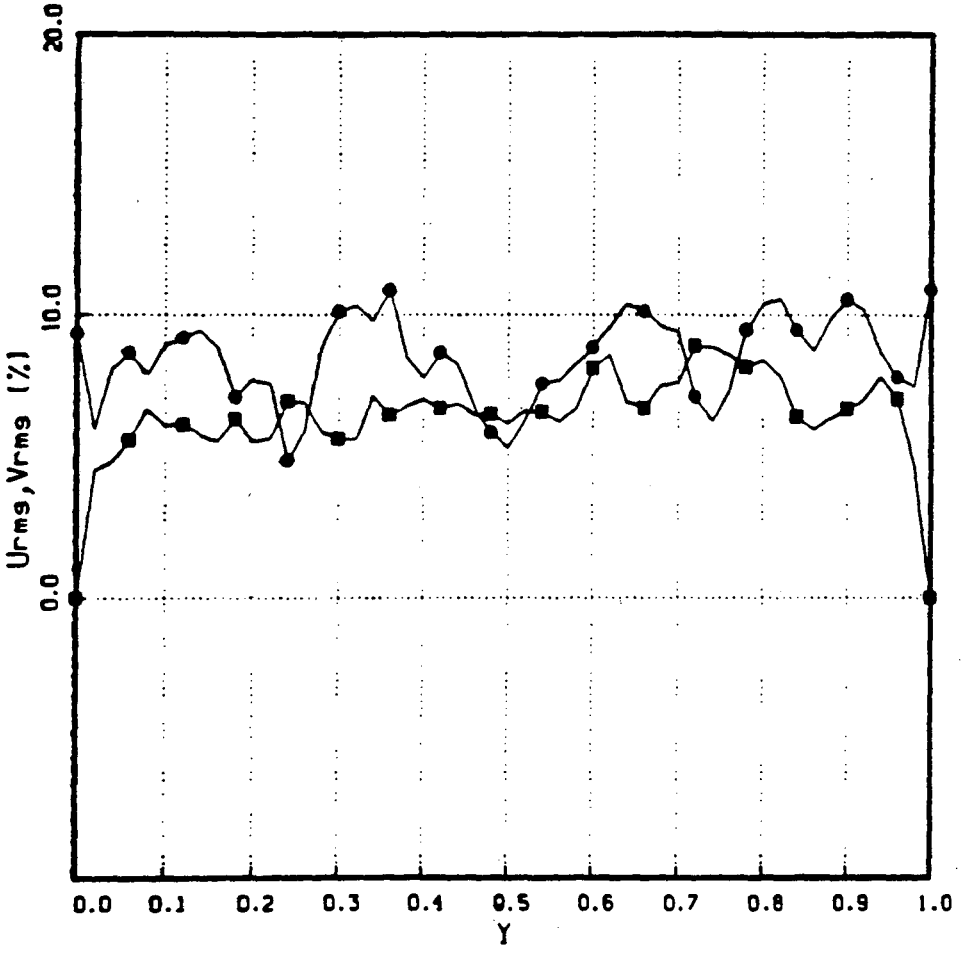

Fig.7 Velocity variances U_{rms} and V_{rms} at x = 0.25, ahead of flameholder.

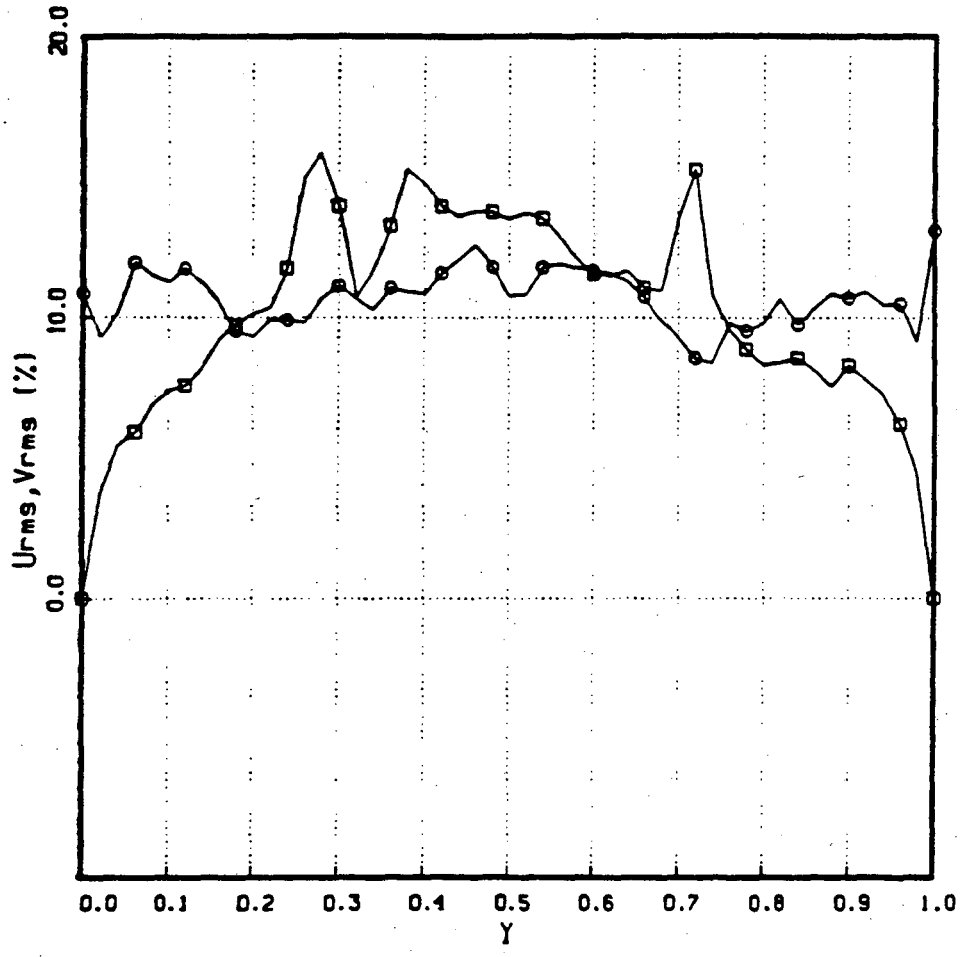

Fig.8 Unconditioned velocity variances U_{rms} and V_{rms} at x =1.0, downstream of flame-holder.

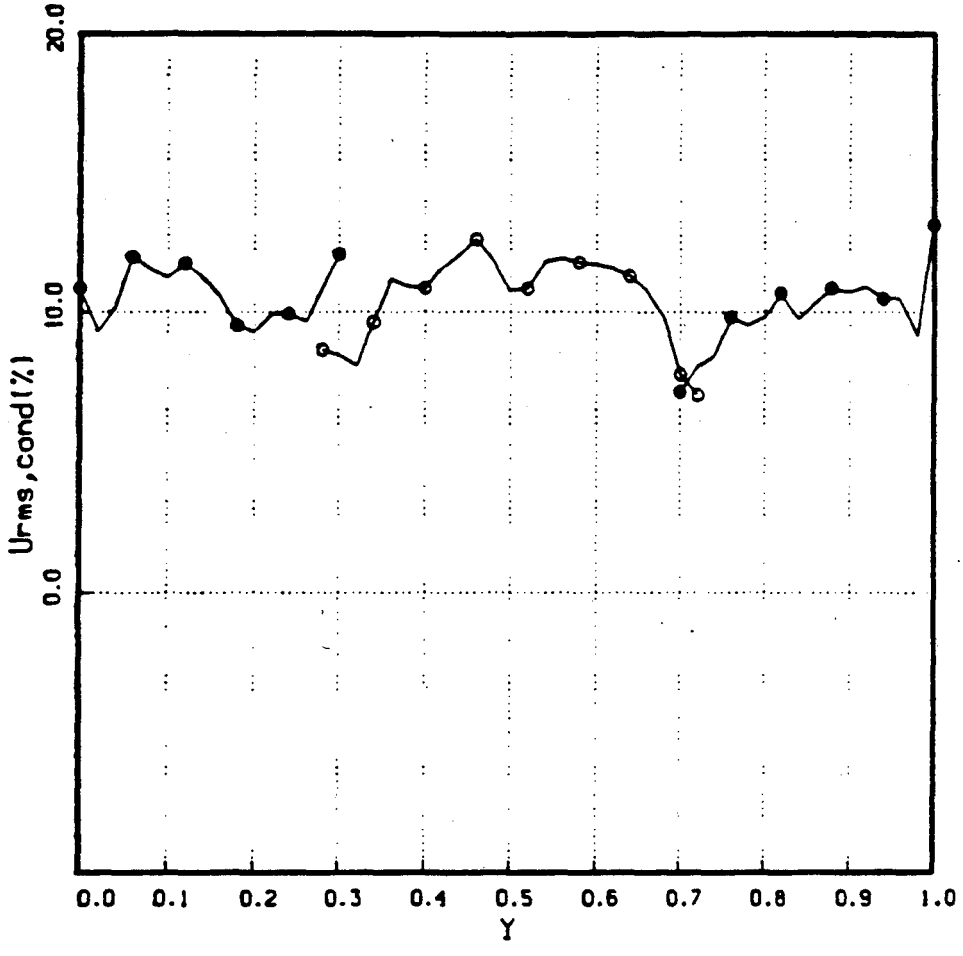

Fig.9 Conditioned variance U_{rms} at x =1.0, in the reactants (filled symbols) and products (open symbols).

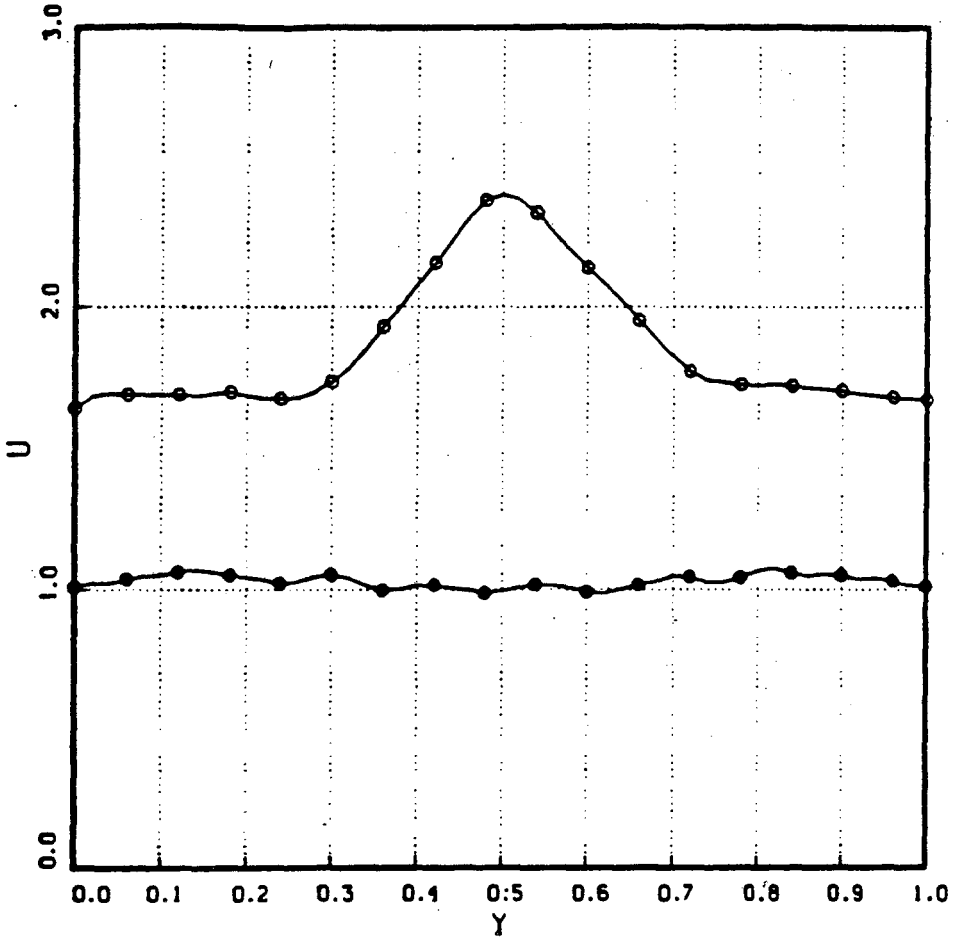

Fig.10 Unconditioned average axial velocity U at x = 0.25 (filled symbols) and x = 1.0 (open symbols).

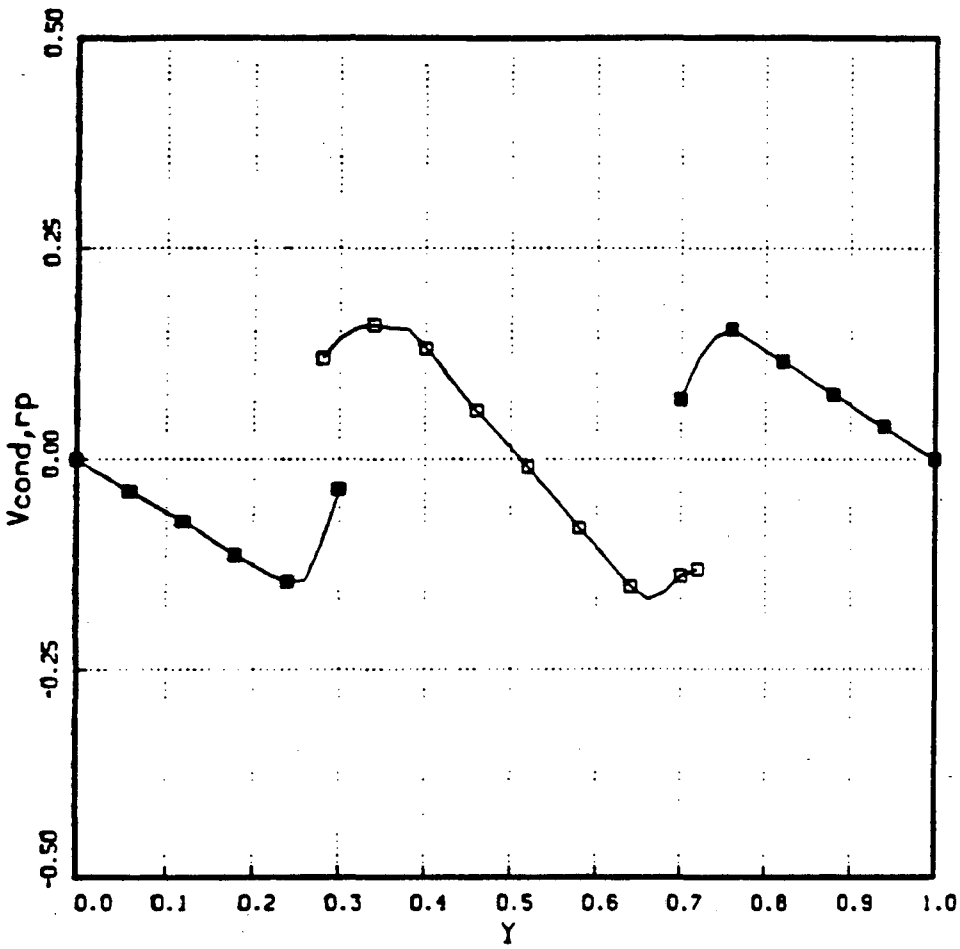

Fig.11 Conditioned average transverse velocity V at x = 1.0 in reactants (filled symbols) and products (open symbols).

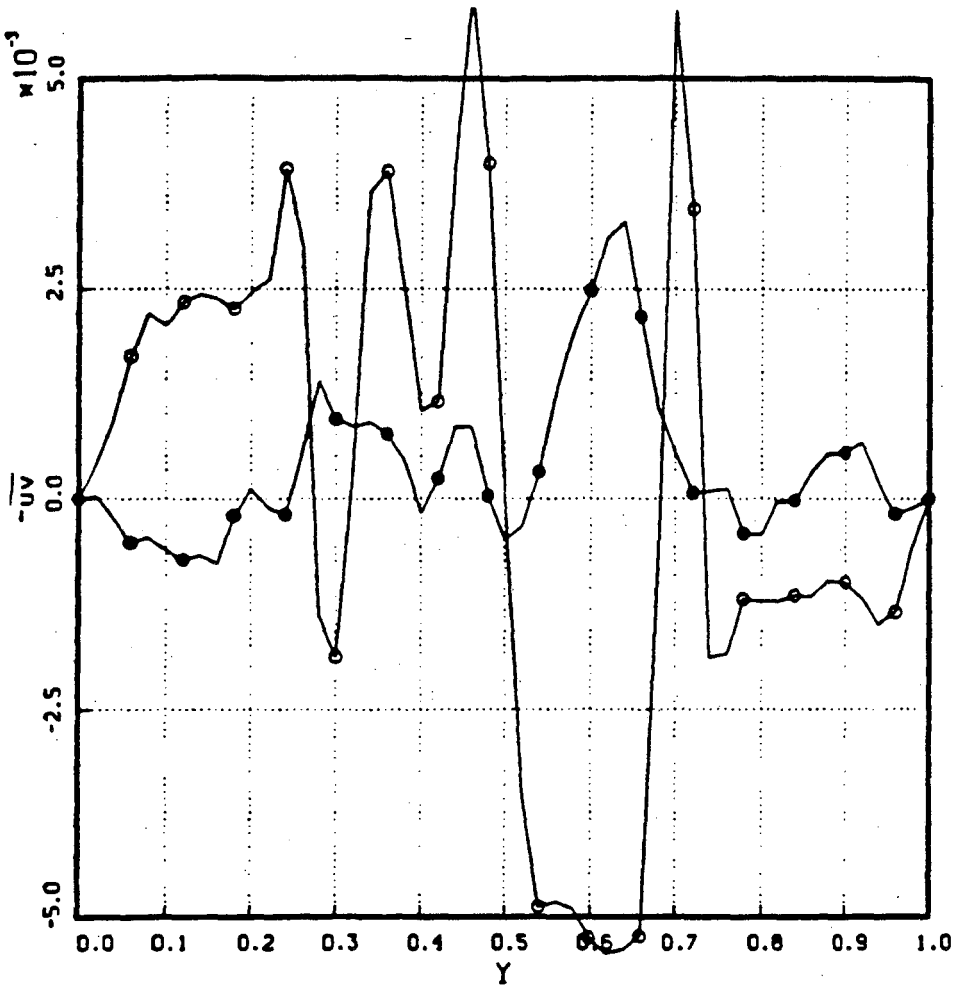

Fig.12 Unconditioned kinematic Reynolds stress at x = 0.25 (filled symbols) and x = 1.0 (open symbols).

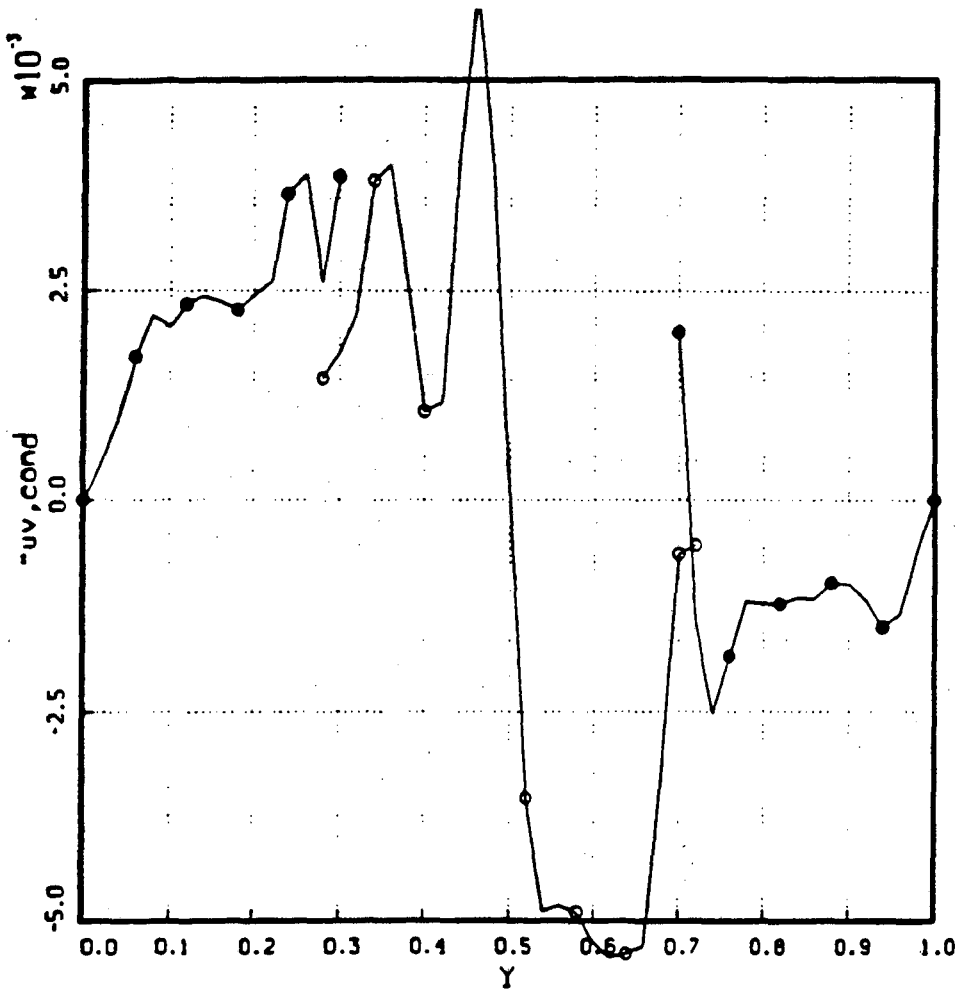

Fig.13 Conditioned kinematic Reynolds stress at $x = 1.0$ in reactants (filled symbols) and products (open symbols).

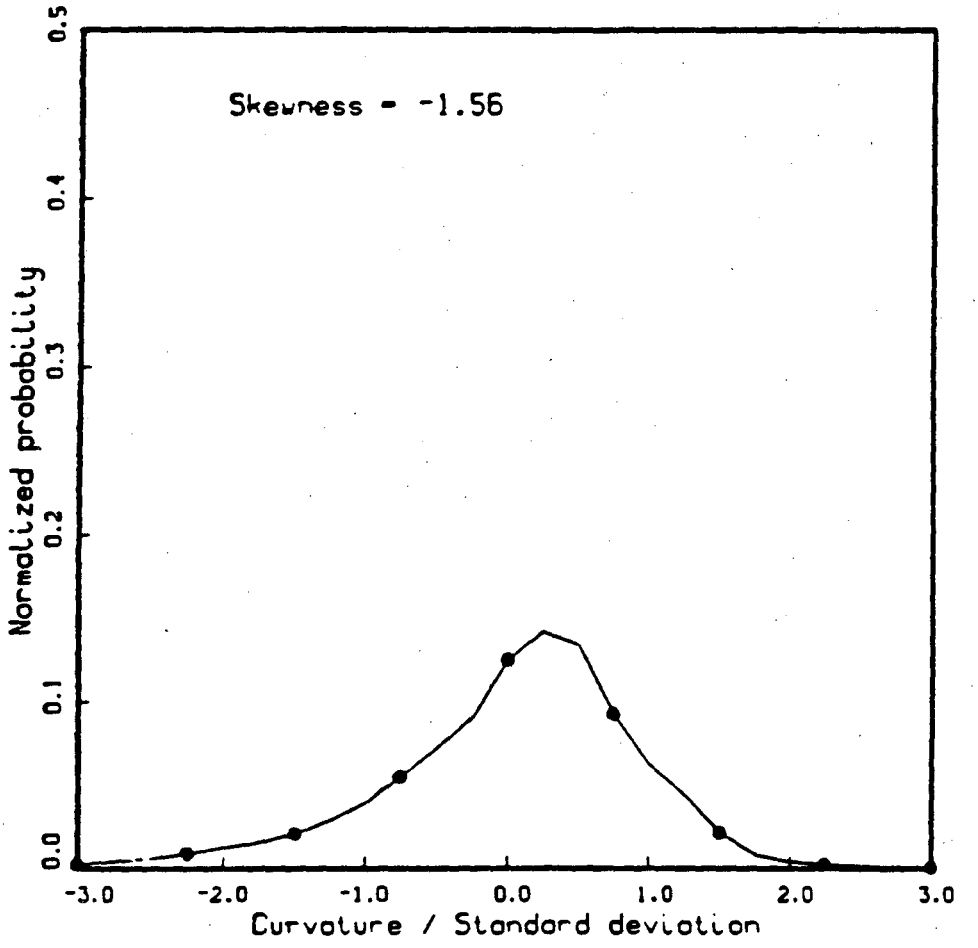

Fig.14 Normalized probability distribution function of flamefront curvature.

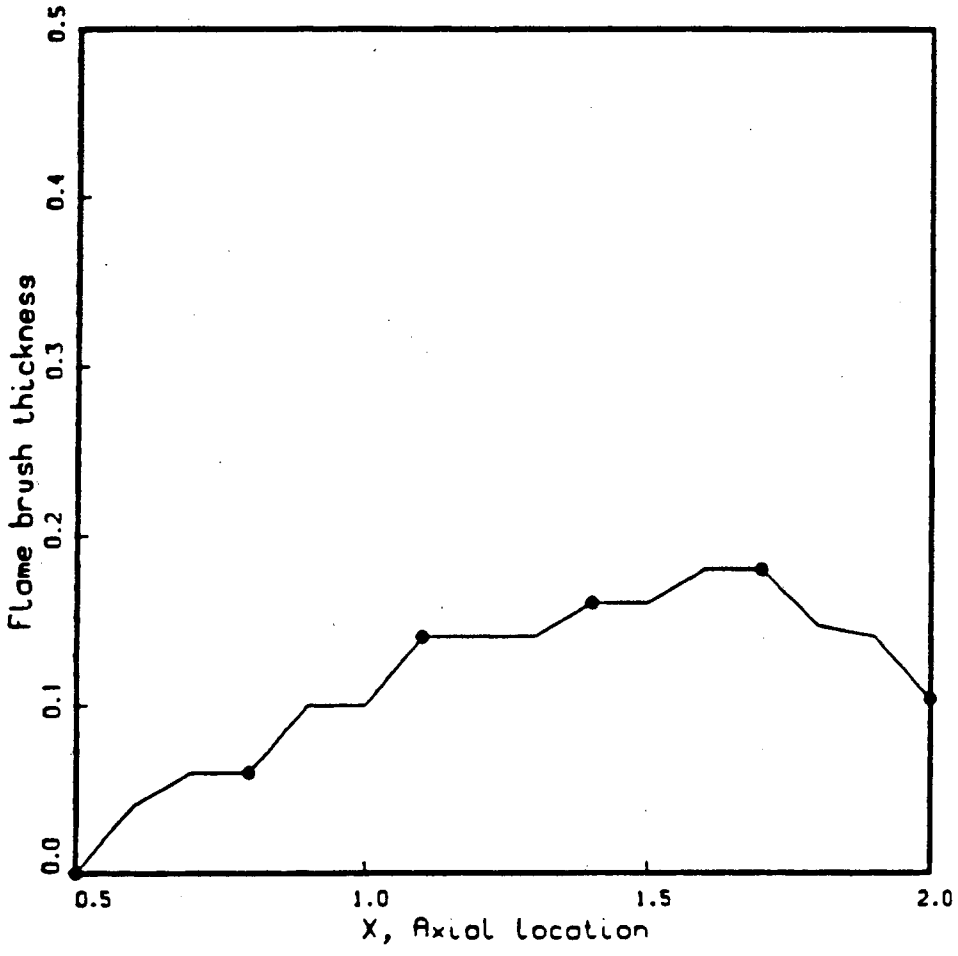

Fig.15 Axial variation of mean flame brush thickness, as defined by the $\langle c \rangle = 0.1$ and $\langle c \rangle = 0.9$ contours.

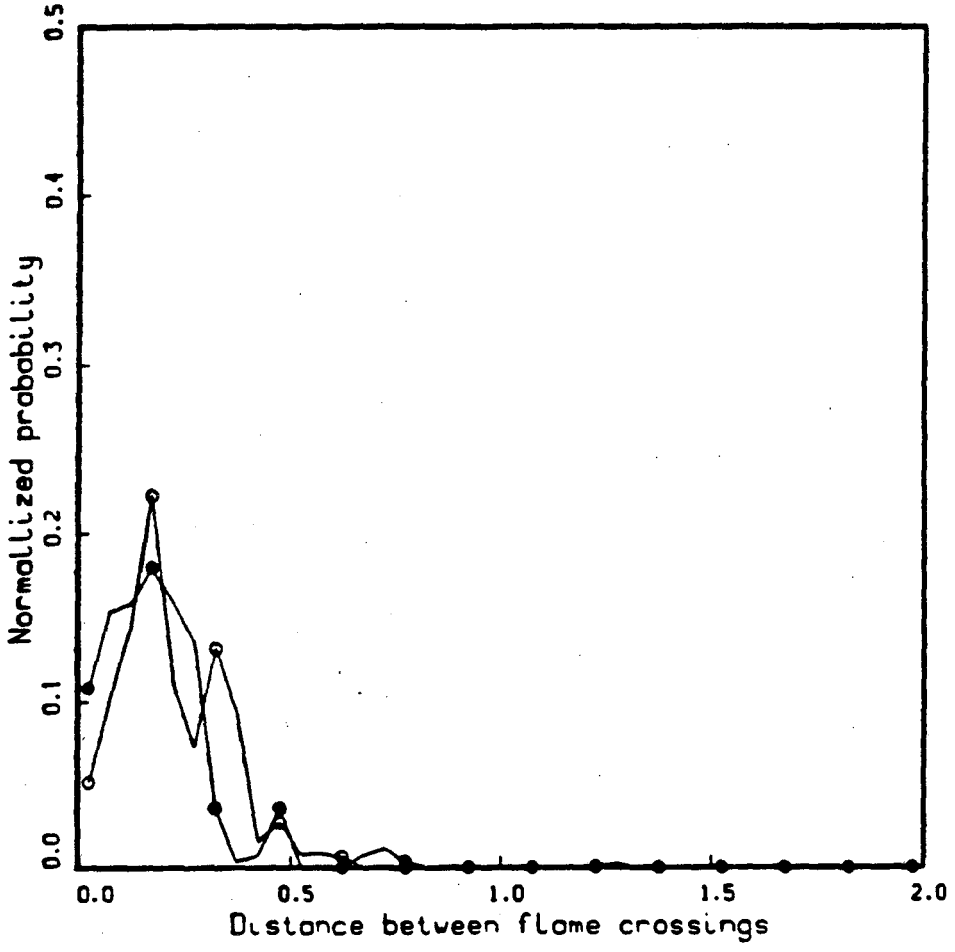

Fig.16 Normalized probability distribution functions of the crossing distances between instantaneous flames and the average flame location $\langle c \rangle = 0.5$ for reactants (filled symbols) and products (open symbols). The similarity of the two pdf's indicates the absence of any significant cusping.

LAWRENCE BERKELEY LABORATORY
UNIVERSITY OF CALIFORNIA
TECHNICAL INFORMATION DEPARTMENT
BERKELEY, CALIFORNIA 94720